

# X-ray spectral and timing evolution during the 2018 outburst of MAXI J1820+070

YaXing Li<sup>1,2</sup>, Zhen Yan<sup>1\*</sup>, ChenXu Gao<sup>1,2</sup>, and Wenfei Yu<sup>1</sup>

<sup>1</sup>Shanghai Astronomical Observatory, Chinese Academy of Sciences, 80 Nandan Road, Shanghai 200030, China

<sup>2</sup>Chinese Academy of Sciences, University of Chinese Academy of Sciences, 19A Yuquan Road, Beijing 100049, China

Accepted 2025 February 24; Received 2025 February 17; in original form 2024 July 6

## ABSTRACT

We made use high-cadence observations from the *Insight*-HXMT and *NICER* to scrutinize the spectral and timing evolution during the 2018 outburst of the black hole X-ray binary (BHXR) MAXI J1820+070. Its hardness-intensity diagram (HID) displays a “q”-like track including all the spectral states, along a unique loop in the hard state. The tracks observed in the HID is anticipated in the evolution of the components responsible for Compton and reflection emission. This is substantiated by the relationship between the X-ray luminosity  $L_X$  and photon index  $\Gamma$  which exhibits a pattern reminiscent of HID. The distinctive evolution of the reflection component leads to the unique loop in the HID (also in the  $L_X$ – $\Gamma$  plane) of hard state. Additionally, we found a negative correlation between frequency of the type-C quasi-periodic oscillation (QPO) ( $\nu_{C,QPO}$ ) and the optical depth of the Compton emission ( $\tau$ ), and a positive correlation between  $\nu_{C,QPO}$  and  $\Gamma$ . These correlations strongly suggest a coupling between the QPO properties and the underlying process responsible for Comptonization. We also found that the last detection of type-C QPO coincide with the transient jet ejection within a timescale of one hour.

**Key words:** accretion, accretion discs – black hole physics – X-rays: binaries – stars: individual: MAXI J1820+070

## 1 INTRODUCTION

The majority of Galactic black hole X-ray binaries (BHXR) behave as transient sources that spend years to decades in a quiescent state. Occasionally, they undergo outbursts lasting for weeks to months before returning to quiescence (Yan & Yu 2015; Corral-Santana et al. 2016). These outbursts may involve transitions through distinct accretion states, which are characterized by a variety of X-ray spectral and timing features, along with associated radio emission (see reviews by Remillard & McClintock 2006; Done et al. 2007; Belloni 2010). Given their proximity at kiloparsec distances and their dramatic variability on timescales spanning from days to months, BHXR serve as excellent targets for real-time monitoring of the accretion flow and jet behavior. High-cadence observations yield valuable insights into the physics of accretion and its interplay with jets across different accretion states.

The outburst usually starts from the hard state (HS) when the luminosity is low. The X-ray spectrum of HS is dominated by Comptonized emission produced from a hot plasma usually called corona (Sunyaev & Truemper 1979), a weak thermal component from the accretion disk is also detected. In this state, the strong low-frequency quasi-periodic oscillations (LFQPOs) and broad line noises (BLNs) are usually detected in the power density spectrum (PDS, e.g. Belloni et al. 2002; Casella et al. 2004). As the outburst goes on, the disk component becomes stronger. When the spectra are dominated by the thermal component from an optically thick disk extending to the innermost stable circular orbit (ISCO) of the BH (Novikov & Thorne

1973; Shakura & Sunyaev 1973), the outburst enters the soft state (SS). In contrast to HS, SS shows low X-ray variability amplitude with a few percent fractional root mean square (RMS), and LFQPOs are rarely detected (Motta et al. 2012). The transition between the HS and SS is called intermediate state (IMS). During the outburst decay, the disk temperature and luminosity decrease. At some point, the corona restrengthens and dominates over the disk component, which indicates the outburst return to HS.

A large fraction of outbursts experience a transition from the HS to SS state (H-S) during the outburst rise, and conversely, from SS to HS (S-H) during the outburst decay (e.g. Yu & Yan 2009; Tetarenko et al. 2016). Through the comprehensive X-ray spectral and timing analysis, we can conduct detailed research on different spectral states and state transitions (e.g. Belloni 2010). Notably, the X-ray spectral and timing properties exhibit pronounced changes during these state transitions, providing valuable insights into the changes in innermost accretion flow and/or jet around the BH. On one hand, the X-ray timing and spectral properties of the BH are closely correlated. The correlations between the QPO frequency and spectral parameters, such as the photon index, disk temperature, and X-ray flux, have been widely studied. Those correlations have been used to investigate the origin of QPOs, accretion geometries across different spectral states, and similarities and/or differences between various BHXR (e.g. Muno et al. 1999; Sobczak et al. 2000; Vignarca et al. 2003; Debnath et al. 2008; Shaposhnikov & Titarchuk 2009; Motta et al. 2011; Stiele et al. 2013). On the other hand, there are many spectral-timing techniques and modeling combine energy spectral and variability information to offer additional perspectives on the accretion and jet during the outburst. For example, phase-lag spectra including lag-

\* E-mail: zyan@shao.ac.cn

frequency spectra and lag-energy spectra are usually used to probe the physical connection of variability in different energy bands (e.g. Uttley et al. 2014; De Marco et al. 2015; Wang et al. 2022b), while RMS spectra are used to study the energy-dependent variability of different signals (e.g. Stiele & Yu 2015; Wang et al. 2022a; Ma et al. 2023b). Additionally, phase-resolved spectroscopy has also been applied to study spectral evolution on the QPO time scale (e.g. Ingram et al. 2016; Stevens & Uttley 2016; Nathan et al. 2022; Gao et al. 2023) and frequency-resolved spectroscopy is utilized to explore the X-ray energy distribution across different short time scales (e.g. Gilfanov et al. 2000; Axelsson & Done 2016).

## 2 MAXI J1820+070

In this work, we focus on the evolution of the very bright outburst of MAXI J1820+070. The X-ray outburst MAXI J1820+070 was first detected by Monitor of All-sky X-ray Image (MAXI) on March 11, 2018 (MJD 58188, Kawamuro et al. 2018). The optical counterpart ASASSN-18ey was discovered by the All-Sky Automated Survey for Supernovae (ASAS-SN) (Shappee et al. 2014) around several days earlier (Tucker et al. 2018; Denisenko 2018). Soon after, the source was classified as a BHXRb according to the follow-up observations in different wavelengths (Baglio et al. 2018; Bright et al. 2018; Uttley et al. 2018). Atri et al. (2020) measured the distance of  $2.96 \pm 0.33$  kpc by using the radio parallax method and a jet inclination angle of  $63 \pm 3^\circ$  with very long baseline interferometry (VLBI) observations. Torres et al. (2020) estimated the mass of black hole is  $8.48^{+0.79}_{-0.72} M_\odot$ . The spin of the BH was estimated as 0.14 (Zhao et al. 2021).

Like other transient BHXRbs, MAXI J1820+070 is in HS at the beginning of the outburst. It is a very long HS, extending until around MJD 58290. Subsequently, the source enters the IMS. The above two periods are referred to as rising HS and IMS states. The transient jet ejected around MJD 58306 (Bright et al. 2020; Wood et al. 2021), coinciding with the transition between hard intermediate state (HIMS) and soft intermediate state (SIMS; Fender et al. 2004). The SS lasts from MJD 58310 to 58383. At about MJD 58393, the source returns to the HS. In order to distinguish from the outburst rise phase, the period between MJD 58383 to 58393 and after are referred to as decaying IMS and HS states, respectively. The time intervals of different spectral states are shown in Figure 1 (see also Shidatsu et al. 2019).

The observations targeted on MAXI J1820+070 during this outburst have been conducted by almost all the active X-ray missions in orbit, such as *AstroSat* (Mudambi et al. 2020), *Chandra* (Espinasse et al. 2020), *Insight-HXMT* (You et al. 2021; Ma et al. 2021), *NICER* (Kara et al. 2019; Wang et al. 2021), *NuSTAR* (Buisson et al. 2019, 2021), *Swift* (Stiele & Kong 2020), *XMM-Newton* (Xu et al. 2020; Dias et al. 2024). Recent studies on the accretion geometry around the black hole in MAXI J1820+070 have made significant strides, yet the conclusions remain a topic of debate. On one hand, the traditional truncated disk/inner hot flow model successfully explains the X-ray spectral and timing properties (e.g. Xu et al. 2020; De Marco et al. 2021; Zdziarski et al. 2022). On the other hand, a jet-like corona with vertical changes has been proposed to explain the spectral and timing evolution during the hard state (e.g. Kara et al. 2019; Wang et al. 2021; You et al. 2021). Additionally, complex corona geometries have been suggested, including two corona components producing Compton emission (Buisson et al. 2019; Zdziarski et al. 2021; Ma et al. 2023a) and a stratified hot flow (Dziefak et al. 2021).

By concurrently applying X-ray spectral and timing analysis dur-

ing this outburst, it is very helpful to uncover the properties and evolution of accretion flows around black holes (e.g. Kara et al. 2019; Stiele & Kong 2020; Wang et al. 2020; De Marco et al. 2021; Kawamura et al. 2023). *Insight-HXMT* is one of the best missions for performing X-ray spectral and timing study in a very broad energy band 1–250 keV (Zhang et al. 2020). It carries three slat-collimated payloads: low energy X-ray telescope (LE, 1–15 keV, Chen et al. 2020), medium energy X-ray telescope (ME, 5–30 keV, Cao et al. 2020) and high energy X-ray telescope (HE, 20–250 keV, Liu et al. 2020). All three instruments have large collecting areas and high time resolution, which are beneficial for conducting X-ray spectral and timing analysis for bright targets. *Insight-HXMT* observed MAXI J1820+070 from March 14, 2018 to October 21, 2018, and obtained a total of more than 310 exposures with an average interval of 0.63 days. The *Insight-HXMT* observations extensively cover the different spectral states through almost the entire outburst Figure 1. We also used the data from *NICER* in some cases. Due to its high time resolution and large effective area, *NICER* data can provide X-ray spectral and timing analysis in the 0.2–12 keV.

## 3 DATA REDUCTION AND DATA ANALYSIS

### 3.1 *Insight-HXMT* data reduction

The *Insight-HXMT* data and products were processed and extracted by using the *Insight-HXMT* Data Analysis Software package (HXMTDAS). We first screened the original event data of three instruments by using `lescreen`, `mescreen` and `hescreen` with the recommended criteria in the user manual<sup>1</sup>. The spectra and light curves were extracted by using the tools `lespecgen`, `mespecgen`, `hespecgen`, `lel1cgen`, `mel1cgen` and `hel1cgen` for the target, and using the tools `lebkgmap`, `mebkgmap` and `hebkgmap` for the background, respectively. All the spectra were grouped with a minimum count of 25 per bin.

The net light curves were calculated with `lcmath`. We then used the `powerspec` in *XRONOS* package to compute the power density spectrum (PDS) in Leahy normalization (Leahy et al. 1983). The net light curves with a time resolution of 1/512 seconds were divided into segments with a length of 512 seconds for producing the PDSs. So the frequency resolution of the PDS is 1/512 Hz and the Nyquist frequency is 256 Hz.

### 3.2 *NICER* data reduction

The raw data were first reprocessed by using task `nicer12` in the *NICER* software package *NICERDAS*. The source and background spectra, ancillary response files (ARFs) and response matrix files (RMFs) were all extracted by using the pipeline task `nicer13-spect`. During the above procedure, the *SCORPEON* background model was chosen, and the recommended systematic error from the calibration file was applied. The spectra were grouped with a minimum count of 25 per bin.

### 3.3 X-ray timing analysis

We excluded the soft state from MJD 58310 to 58383 for timing analysis of *Insight-HXMT* data. The PDSs were then logarithmically re-binned with an increment factor of 0.025 in frequency and

<sup>1</sup> <http://hxmtcn.ihep.ac.cn/SoftDoc.jhtml>

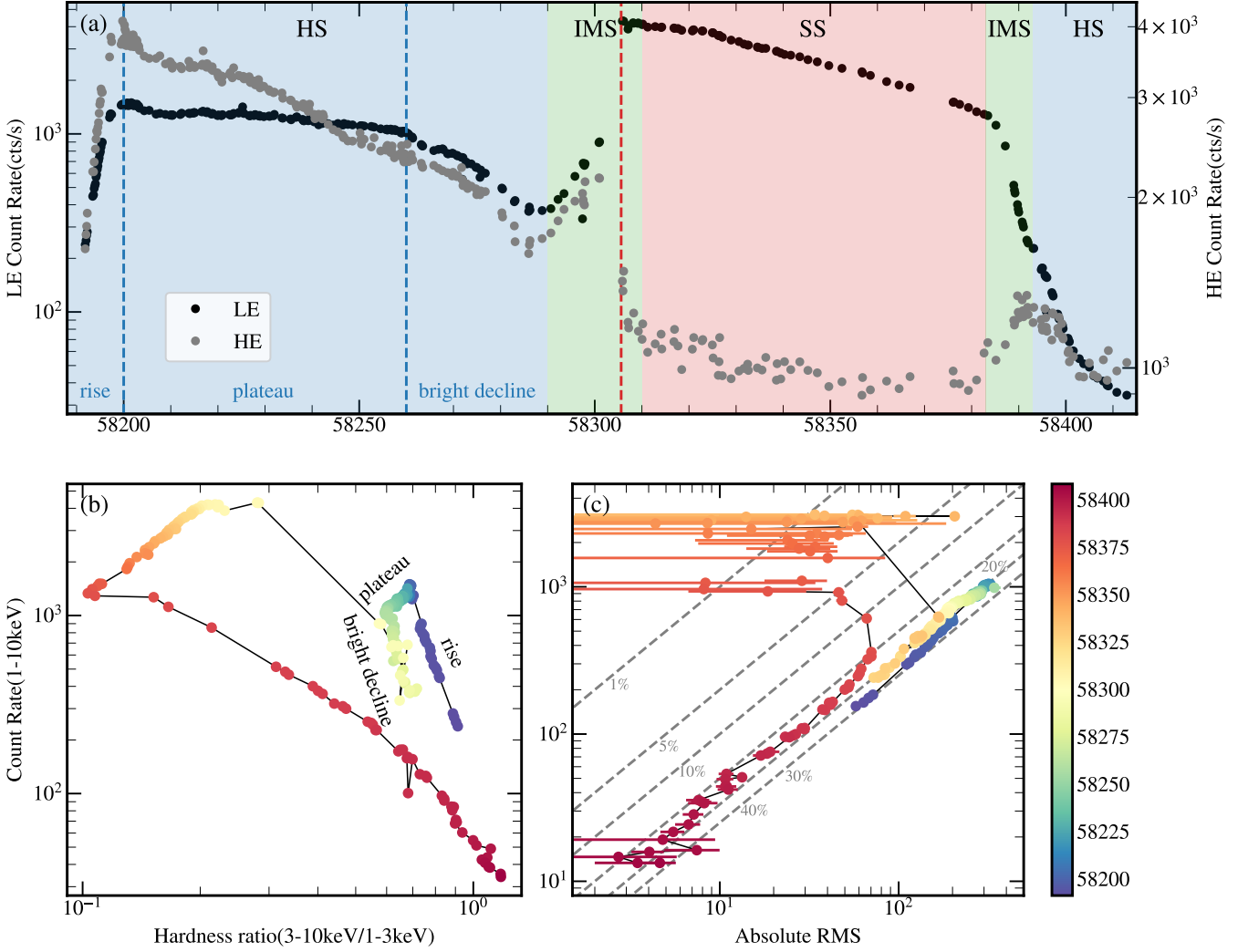


**Figure 1.** *Insight*-HXMT light curve, hardness-intensity diagram and absolute RMS-intensity diagram of MAXI J1820+070 during the 2018 outburst. (a) Light curves obtained from LE and HE of *Insight*-HXMT. The colors of the background represent the spectral states: blue for the hard state, green for the intermediate state and red for the soft state. The blue dashed lines separate three phases of the rising hard state: the rise, plateau and bright decline phases. The red dashed line marks the transient jet ejection time MJD 58305.60 according to Wood et al. (2021) and also the boundary between HIMS and SIMS. (b) The *Insight*-HXMT hardness-intensity diagram, defined as the total 1–10 keV count rate vs. the ratio of hard (3–10 keV) to soft (1–3 keV) count rates. The three phases of the rising HS correspond to the three curves of the small “ $\eta$ ”-like track on the upper right. (c) The absolute RMS-intensity diagram, with the grey lines corresponding to the values of fractional RMS. Both absolute RMS and fractional RMS are determined in the 0.1–64 Hz from *Insight*-HXMT/LE PDS. The color bar on the right corresponds to the observation time.

formatted to be compatible with XSPEC (Ingram & Done 2012). We then used a combination of Lorentzian functions and a constant to fit the PDSs in XSPEC (v12.12.1): two or four Lorentzians for the BLNs, two or three Lorentzians for the QPO and its harmonic and/or subharmonic and a constant for the white noise. The PDS of the data from LE and ME detectors on the *Insight*-HXMT can be described by a QPO and two BLN components, while the data from HE detectors will use two additional Lorentzians to supply the BLN components.

Some *NICER* observations during the IMS were used since the *Insight*-HXMT observation was absent during the period of MJD 58301–58305 (obsID 1200120192–1200120197). The *NICER* PDSs consist of one to three BLN components and one or two QPO components. The uncertainties of all parameters were calculated from the Markov Chain Monte Carlo (MCMC) method by the implementa-

tion of emcee in XSPEC<sup>2</sup>. Some examples of PDSs fitting are shown in Figure C4. Using the best-fitting results of PDSs, we calculated the fractional RMS =  $\sqrt{K/\langle x \rangle}$ , where  $K$  is the normalization of the Lorentzian function and  $\langle x \rangle$  is the mean count rate (Leahy et al. 1983; van der Klis 1989).

### 3.4 X-ray spectral analysis

We performed the spectral fitting through XSPEC v12.12.1 using the chi statistic. Different models were applied in different spectral states. During the hard state of the outburst rise phase, we applied the model

<sup>2</sup> [https://github.com/zoghbi-a/xspec\\_emcee](https://github.com/zoghbi-a/xspec_emcee)

constant\*TBabs\*(thcomp\*kerrd+relxillCp+xillverCp) to fit X-ray spectra in the 2–150 keV. The constant factor was used to coordinate the calibration differences between different instruments, where the constant for LE was fixed at 1. The equivalent hydrogen column density ( $N_H$ ) of TBabs was fixed at  $0.15 \times 10^{22} \text{ cm}^{-2}$  (Uttley et al. 2018). The kerrd is a standard optically thick accretion disk model for a Kerr black hole (Ebisawa et al. 2003), which accounts for the accretion disk radiation. We adopted thcomp to describe the Comptonization emission from the corona, where the seed photons come from the accretion disk. And relxillCp (version 2.3) is a relativistic reflection model that calculates the reflection spectrum from an accretion disk illuminated by the corona (García et al. 2014; Dauser et al. 2022), while xillverCp was used to account for a further away and non-relativistic reflection component (e.g. Buisson et al. 2019; You et al. 2021). In our spectral fitting, we fixed the black hole spin at  $a = 0.14$  (Zhao et al. 2021), the inclination angle at  $i = 63^\circ$  (Atri et al. 2020), the distance at 2.96 kpc (Atri et al. 2020) and the black hole mass at  $8.48 M_\odot$  (Torres et al. 2020). Additionally, Tcol/Teff in kerrd was fixed at 1.7 (Shimura & Takahara 1995). We tied the inner disk radius  $R_{\text{in}}$  (in units of  $R_g$ ) in relxillCp to that in kerrd. For simplicity, we used a continuous power-law emissivity and fixed the index at  $q_1 = q_2 = 3.0$ , and a constant ionization (iongrad\_type=0) in relxillCp. In particular, the reflection fraction refl\_frac in relxillCp and xillverCp were set at -1 to acquire the reflection component.

Furthermore, we used cflux to get the X-ray flux of different spectral components in the 0.1–100 keV range. Notably, the X-ray flux of the Comptonization component can be calculated as  $F_C = F_{\text{thcomp*kerrd}} - (1 - \text{cov\_frac}) * F_D$ , where  $F_{\text{thcomp*kerrd}}$  is the integrated flux of the convolution between thcomp and kerrd components. The total reflection flux is the sum of relativistic reflection flux and non-relativistic flux. However, the non-relativistic component in the IMS is weak and cannot be well constrained; therefore, we only used the relxillCp during this period. During and after the soft state, we applied the model constant\*TBabs\*thcomp\*kerrd to fit the broadband X-ray spectrum. The electron temperature  $kT_e$  is fixed at 100.0 keV. For some observation during the decaying HS, the covering fraction cov\_frac is fixed at 1 (see Figure 2). Then, we also used cflux to calculate the flux of the disk and Comptonization component in 0.1–100 keV energy range. The uncertainties of all the parameters were calculated from the MCMC method using the emcee in XSPEC. All the spectra can be well fitted by our models across different spectral states. We show some examples of energy spectra fitting in Figure C4.

Because of the absence of *Insight*-HXMT observation around MJD 58301 to 58305 in the IMS, we used the *NICER* data as the supplementary. Then we applied the same model as used for *Insight*-HXMT data during this period to fit the spectra in the 1.5–10 keV: constant\*TBabs\*(thcomp\*kerrd+relxillCp). For simplicity, we fixed the electron temperature  $kT_e$  at 100.0 keV for those *NICER* observations. We checked the simultaneous *NICER* and *Insight*-HXMT observations before and after this period. The main spectral parameters are almost similar during the HIMS (see section B in detail).

## 4 X-RAY SPECTRAL AND TIMING EVOLUTION DURING THE 2018 OUTBURST

### 4.1 Unique evolution of rising HS

The count rates of MAXI J1820+070 from LE and HE of *Insight*-HXMT are plotted in Figure 1a, and the hardness-intensity diagram (HID) and absolute RMS-intensity diagram (RID) are also shown in Figure 1b and c. The light curve of MAXI J1820+070 shows a multi-peaked outburst profile (Chen et al. 1997). The first peak remains in the hard state, while its HID exhibits a small loop, which looks like a “ $\eta$ ” track (Figure 1b). The rising HS is divided into three phases: the rise, plateau and bright decline phases (e.g. Stiele & Kong 2020; De Marco et al. 2021), which roughly corresponds to the three curves of the small “ $\eta$ ”. The rise phase is from the start of the outburst to MJD 58200 when the count rate reaches the peak and then begins to decrease slowly. The plateau phase is from MJD 58200 to 58260, and the bright decline phase is from 58260 to MJD 58290. The energy spectra and PDSs in different phases are shown in Figure C4. The absolute RMS and count rate do not follow a single positive correlation (Figure 1c; see also Stiele & Kong 2020). This loop evolution of rising HS in HID/RID has never been shown in other BHXRBs (Belloni 2010; Belloni & Motta 2016). Even in other outbursts with multiple peaks, their HID/RID usually do not show a loop trend during the rising HS, such as the outbursts in XTE J1550–564, GX339-4 and GRO J1655–40 (e.g. Sobczak et al. 2000; Debnath et al. 2008; Clavel et al. 2016).

During the rising HS, our timing and spectral analysis results show a clear distinction between this special plateau phase and the rise and bright decline phases. Notably, despite the gradual decline of the HE count rate during the plateau phase, the Comptonization luminosity  $L_C$  remains almost unchanged. The mass accretion rate  $\dot{M}$  and disk luminosity  $L_D$  also remain stable during the plateau phase. The evolution trends observed in  $\Gamma$ ,  $\dot{M}$  and cov\_frac differ between these three phases of HS. The QPO frequency  $\nu_{C,QPO}$  exhibits a positive and parallel correlation with the total X-ray luminosity  $L_X$  during the rise and bright decline phases while the correlation is negative in the plateau phase (see Figure 7a).

### 4.2 X-ray luminosity and spectral parameter evolution

Based on spectral analysis, we present the evolution of the main parameters of the models in Figure 2. The inner disk radius  $R_{\text{in}}$  steadily decreases during the HS. However, it increases during the IMS and then decreases to the stable value of SS. The photon index  $\Gamma$  manifests different growth rates in the rise and plateau phases of HS, followed by a decrease during the bright decline phase and a rapid increase during the IMS. The electron temperature  $kT_e$  rapidly decreases in the rise phase of HS, then gradually increases until the end of HS. During the IMS, it goes down and up. The mass accretion rate  $\dot{M}$  increases in the rise phase of HS and remains almost stable in the plateau phase, then decreases in the bright decline phase. Subsequently, it increases during the IMS. The cov\_frac which represents the ratio of Comptonized seed photons slowly rises in the HS and rapidly declines in the IMS.

During the SS, the  $\dot{M}$  decreases exponentially accompanied by a relatively constant  $R_{\text{in}}$ .  $\Gamma$  at an early stage of SS is lower than that in SIMS, which demonstrates that there is a strong hard X-ray tail in the *Insight*-HXMT spectra (see also Fabian et al. 2020; Mummery et al. 2024). The  $\Gamma$  is fixed at 2.4 for the rest of SS. During the decaying IMS,  $\Gamma$  gradually drops to the HS level  $\sim 1.7$ . The cov\_frac remains at almost zero value during the SS and increases to the HS level in the

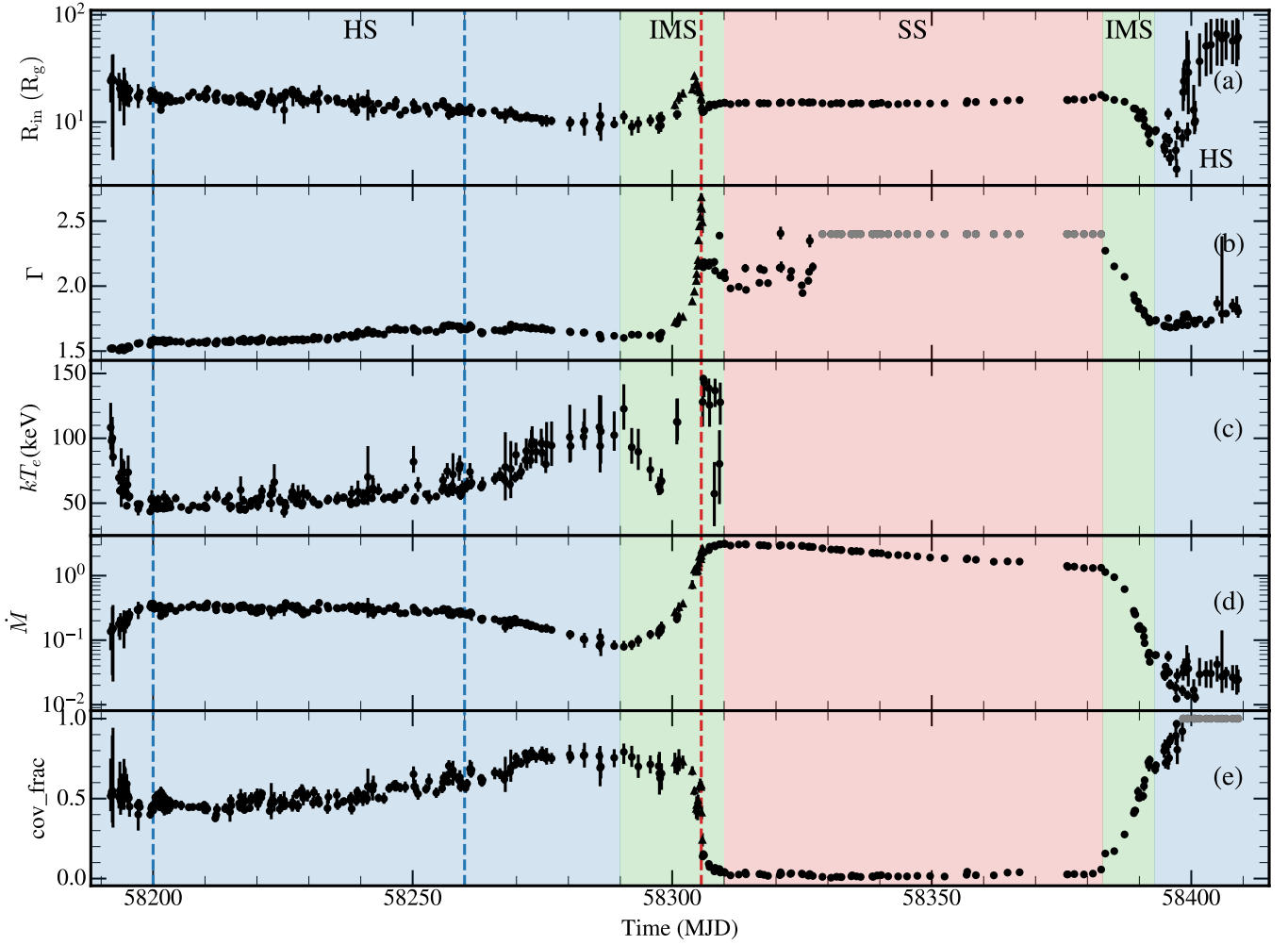


**Figure 2.** Time evolution of spectral parameters. From top to bottom: the inner disk radius  $R_{\text{in}}$ , the photon index  $\Gamma$ , the electron temperature  $kT_e$ , the mass accretion rate  $\dot{M}$ , the cover fraction `cov_frac`. The dots are derived from *Insight*-HXMT data and the triangles are derived from *NICER* data. The grey dots represent the fixed values. The colors of the background and dashed lines are the same as in Figure 1.

decaying IMS. The evolution of the spectral parameters in different spectral states is also reported in You et al. (2021); Peng et al. (2023); Fan et al. (2024).

The X-ray luminosity of different spectral components calculated in the energy range of 0.1–100 keV is presented in Figure 3, including the total X-ray luminosity  $L_X$ , the reflection luminosity  $L_R$ , the Compton luminosity  $L_C$ , and the disk luminosity  $L_D$ . In the rise phase of HS, the luminosities of all spectral components increase. Subsequently,  $L_R$  and  $L_X$  decrease until the end of HS. We calculated the ratio of  $L_R$  to  $L_C$  in 20–40 keV energy band as the reflection strength  $R_s$  (Dauser et al. 2016), which increases to the peak synchronously with  $L_R$  during the rise phase of HS and then decreases during the plateau and bright decline phases. Notably,  $L_C$  and  $L_D$  remain stable during the plateau phase and then decrease in the bright decline phase of HS. During the rising IMS, there is a significant increase in luminosities of different spectral components, particularly before the period of transient jet ejection (Figure 3).  $L_D$  exhibits an exponential decline during the SS, then continues to decrease at a steeper rate during the decaying IMS and HS, while  $L_C$  experiences a small flare (Figure 3).

#### 4.2.1 Relationships between $L_X$ and spectral parameters

We then investigated the relationships between X-ray luminosity and the spectral parameters. The relationship between photon index  $\Gamma$  and total X-ray luminosity  $L_X$  is presented in Figure 4a. It is evident that  $L_X$  and  $\Gamma$  show almost identical “q”-like evolution with HID even the small “ $\eta$ ”-like track during the rising HS. The reflection component during the HS of MAXI J1820+070 is very strong, especially during the plateau phase, which is almost the strongest among BHXRBs at the same luminosity (You et al. 2023). Notably, the slope of the reflection spectra in the 2–10 keV energy range are always steeper than that of the Compton spectra (Figure C1), resulting in a larger  $\Gamma$  and also hardness. So the photon index (also hardness ratio) during the plateau phase is seriously influenced by the reflection component. Especially when the reflection component surpasses the Compton component below the energy of the reflection hump in the spectra, the photon index is determined by the reflection component rather than the Compton component (Figure C1). So the distinctive evolution of reflection component leads to the unique “ $\eta$ ”-like track in  $L_X$ – $\Gamma$  and HID during the rising HS.

The relationships between total X-ray luminosity  $L_X$  and both the

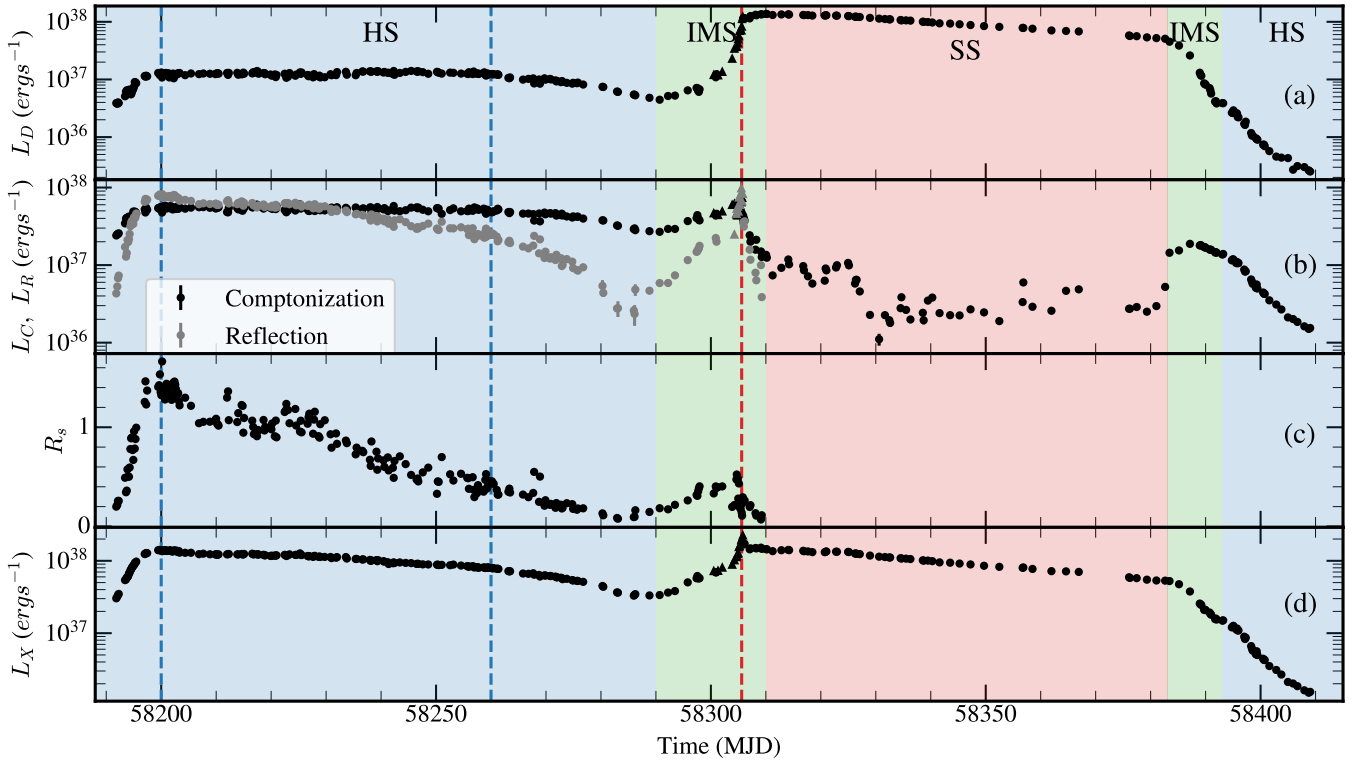


**Figure 3.** Time evolution of X-ray luminosities in 0.1–100 keV of different spectral components: the disk luminosity (a), the Comptonization luminosity and the reflection luminosity (b) and total luminosity (d). We present the reflection strength  $R_s$  at (c), calculated as the ratio of  $L_R$  to  $L_C$  in 20–40 keV energy band. The dots are derived using *Insight*-HXMT data and the triangles are derived using NICER data. The colors of the background and dashed lines are the same as in Figure 1.

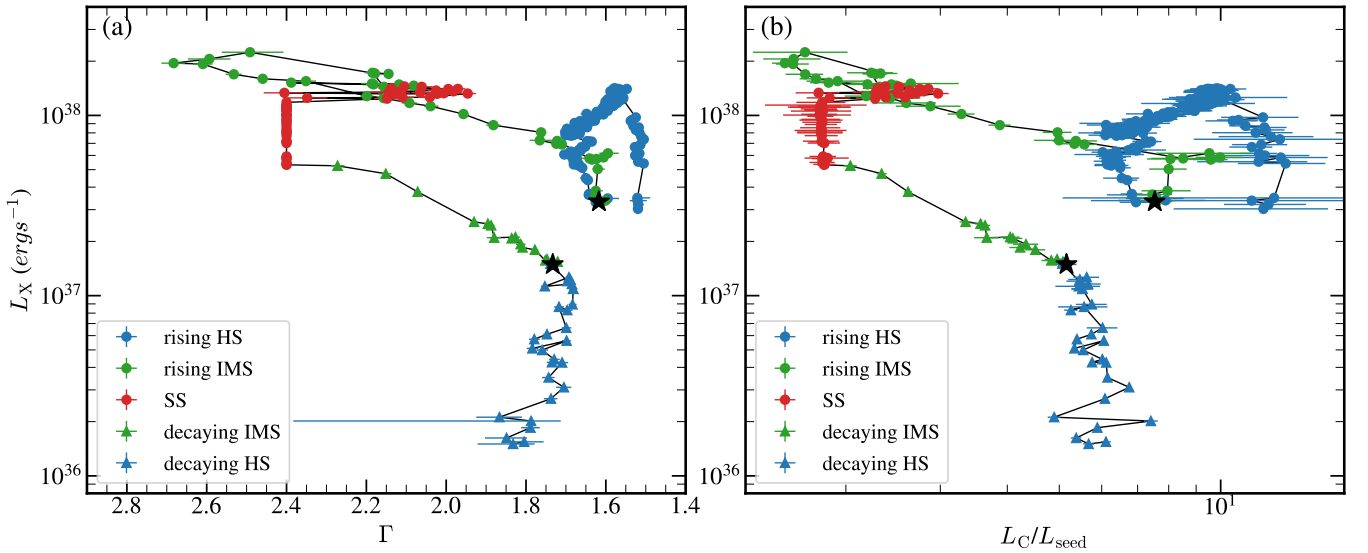


**Figure 4.** (a) The relationship between photon index  $\Gamma$  and total luminosity  $L_X$  during the 2018 outburst. Blue dots, green dots, red dots, green triangles and blue triangles respectively indicate rising hard state and intermediate state, soft state, decaying hard state and intermediate state. The black stars mark the transition luminosities between HS and IMS in the outburst rise and decay phases. Arrows indicate the direction of evolution. (b) The relationship between the ratio of Comptonization luminosity  $L_C$  to seed photons luminosity  $L_{seed}$  and total luminosity  $L_X$  during the 2018 outburst. Symbols and colors are the same as in panel (a).

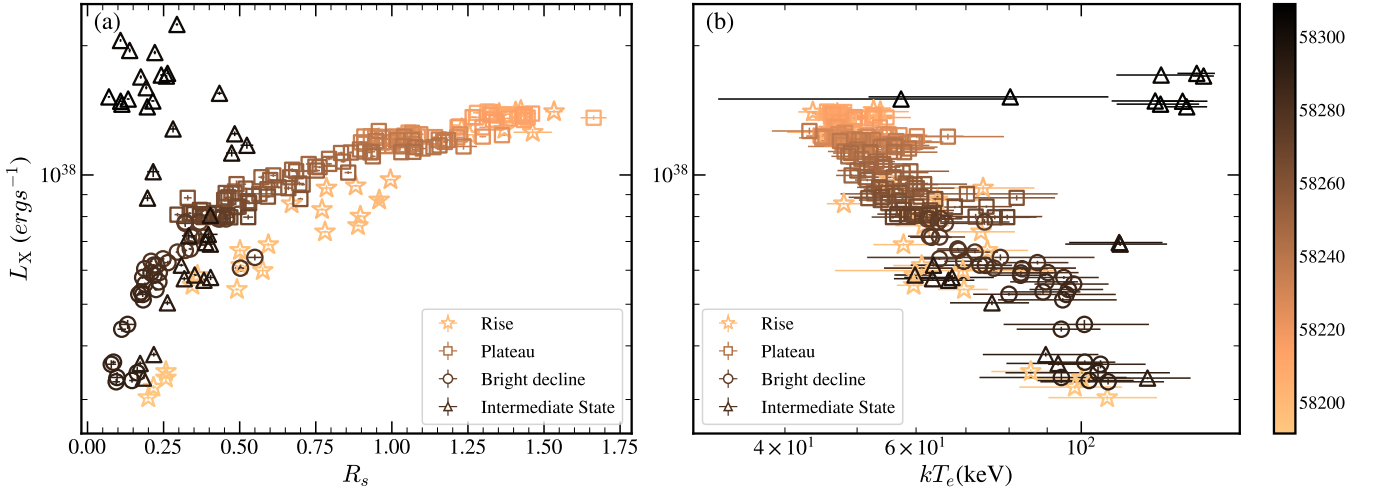


**Figure 5.** (a) The relationship between the reflection strength  $R_s$  and total luminosity  $L_X$  during the hard/hard-intermediate state. The stars, squares, dots and triangles respectively indicate the rise, plateau and bright decline phases in the hard state and intermediate state. (b) The relationship between the electron temperature  $kT_e$  and total luminosity  $L_X$  during the hard/hard-intermediate state. Symbols and colors are the same as in panel (a). The color bar on the right corresponds to the observation time.

reflection strength  $R_s$  and electron temperature  $kT_e$  are respectively shown in Figure 5a and Figure 5b. During the rising HS and HIMS, a positive correlation is observed between  $L_X$  and  $R_s$ , which is not hold in the SIMS (see also You et al. 2023). Concurrently,  $kT_e$  demonstrates a negative correlation with  $L_X$  during both the HS and HIMS (e.g. Yan et al. 2020; You et al. 2023). The observations in SIMS deviates from this relationship.

### 4.3 Type-C QPO evolution

The evolution of centroid frequency of type-C QPO is present in Figure 6. We could detect the type-C QPO from around MJD 58193.42 until MJD 58305.61 when the source reaches the SIMS. The centroid frequency of QPO  $\nu_{C,QPO}$  ranges from 0.01 to 8.05 Hz and the values obtained from the same exposure ID in different detectors (LE, ME and HE) are nearly identical. The  $\nu_{C,QPO}$  evolution obtained from *Insight*-HXMT is almost the same as that from *NICER* data (Stiele & Kong 2020).

The QPO frequency apparently changes at different rates during different phases (Figure 6). Buisson et al. (2018) has claimed that the QPO frequency exponentially increases with time. We also used exponential function  $\nu_{C,QPO} = p_0 e^{(t-t_0)/\tau}$  to fit the  $\nu_{C,QPO}$  at different phases. The best-fitting  $e$ -folding time scales  $\tau$  are  $7.63 \pm 0.78$ ,  $23.99 \pm 0.65$ ,  $-50.27 \pm 7.86$  days for the rise, plateau and bright decline phases of HS, respectively (Figure 6). The  $\nu_{C,QPO}$  evolution during the IMS obviously experiences two different increasing rates with  $e$ -folding time scales of  $8.28 \pm 0.76$ , and  $1.02 \pm 0.05$  days (Figure 6).

We also performed timing analysis for the *Insight*-HXMT data during the decaying IMS and HS. However no significant QPO signals were detected. We noticed that there are some QPO detections with *NICER* data reported in Stiele & Kong (2020). However, only six QPO signals are considered to be significant ( $> 3\sigma$ ). Their frequency and fractional RMS vary chaotically. Consequently, it is difficult to conclusively determine the type and evolution of the detected QPOs during the decaying IMS and HS.

We then investigated the relationships between type-C QPO fre-

quency  $\nu_{C,QPO}$  and spectral parameters during the rising HS and HIMS (Figure 7). The  $\nu_{C,QPO}$  exhibits a complex correlation with the total X-ray luminosity  $L_X$ . Two positive correlations parallelly exist in the rise and bright decline phases of HS and HIMS. However, a negative correlation is observed in the plateau phase of HS (Figure 7a). The  $\nu_{C,QPO}$  and photon index  $\Gamma$  exhibit an overall positive correlation in the HS and HIMS, with varying slopes across different phases (Figure 7b). It appears that the slopes during the rise, plateau, and bright decline phases of HS and HIMS differ. We also calculated the optical depth  $\tau$  of Compton component from  $kT_e$  and  $\Gamma$  according to the equation in (Zdziarski et al. 1996). As present in Figure 7c, the  $\nu_{C,QPO}$  and  $\tau$  roughly follow a negative correlation except the observations in the rise phase of HS. The best-fitting slope of this correlation is obtained as  $-0.96 \pm 0.05$  using the Bayesian method in Buchner (2021). However, the correlation displays a large scatter, with a value of  $0.30 \pm 0.02$ .

### 4.4 Dramatic spectral and timing changes around the transient jet ejection

Dramatic changes of X-ray spectral and timing coincides with transient jet ejections around MJD 58306 (Bright et al. 2020; Homan et al. 2020; Wood et al. 2021). Due to the extensive coverage of *NICER* observation, we are able to investigate the spectral and timing variation before and after the ejection. We divided the two observations (ObsID 1200120196 and 1200120197) around transient jet ejection into 12 segments. The parameters of QPOs detected in each segment are listed in Table C. The frequency of type-C QPO increases until the last detected frequency reaches 8.05 Hz. Notably, the last detection of type-C QPO just coincides with the transient jet ejection on MJD  $58305.60 \pm 0.04$  (Figure 8). Additionally, a type-B QPO around 4 Hz emerges roughly 0.4 days before this ejection. It is first detected on MJD 58305.22 and persists for approximately 13 hours. Although the type-B QPOs are not prominently visible in the dynamic PDSs prior to the ejection (see Homan et al. 2020), they are significantly detected in the averaged PDS of certain segments (Table C).

We also generated the energy spectra for each segment. In spectral

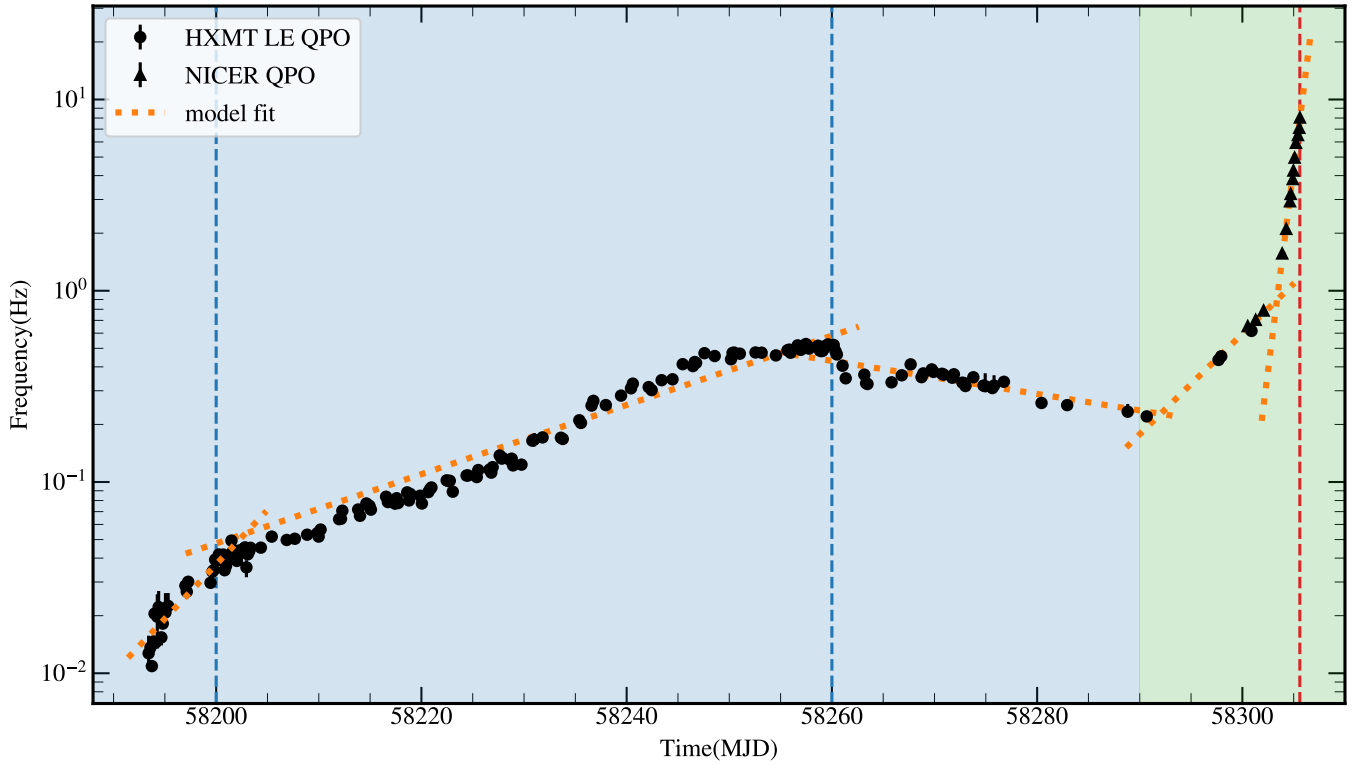


**Figure 6.** Time evolution of the characteristic frequencies of the type-C QPO. The dots are obtained from *Insight*-HXMT LE data and triangles are from *NICER* data. The orange dotted lines represent the best-fitting exponential functions applied to the data of different phases: the rise, plateau, and bright decline phases in hard state, and two segments separated on MJD 58303 during hard intermediate state. The colors of the background and dashed lines are the same as in Figure 1.

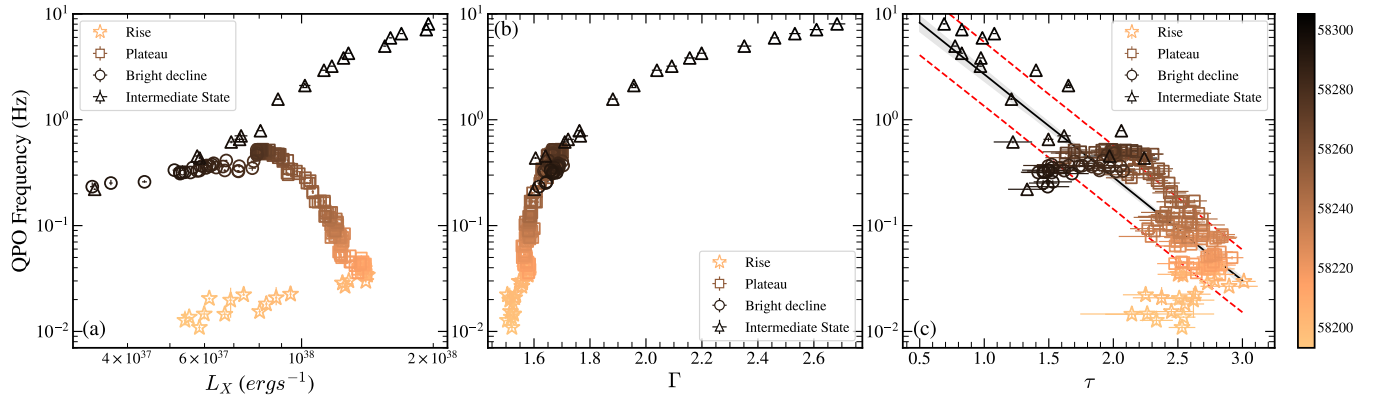


**Figure 7.** (a) The relationship between type-C QPO frequency and total luminosity  $L_X$ . (b) The relationship between type-C QPO frequency and photon index  $\Gamma$ . (c) The relationship between type-C QPO frequency and optical depth  $\tau$ . The black line indicates the best-fitting linear function. The gray shaded area represents the error region for the slope and offset. The red dashed lines indicate the scattering range of the data. Symbols and colors are the same as in Figure 5. The color bar on the right corresponds to the observation time.

fitting, we fixed the electron number density  $\log N$ , iron abundance  $A_{\text{Fe}}$  and ionization parameter  $\log \xi$ . After the transient jet ejection,  $L_C$  drops by a factor of 2 within 8 hours, and  $\text{cov\_frac}$  rapidly decreases to the level of SS.

## 5 DISCUSSION

### 5.1 The “q”-like HID and the evolution of $L_X$ - $\Gamma$

Similar evolution tracks are anticipated in both the  $L_X$ - $\Gamma$  and HID, as the calculated hardness (3–10keV/1–3keV) depends on the slope of the X-ray spectrum, also known as the photon index. Figure 4a displays a “q”-like track between  $L_X$  and  $\Gamma$  when all data from the entire outburst are included, and a small “ $\eta$ ”-like track during the

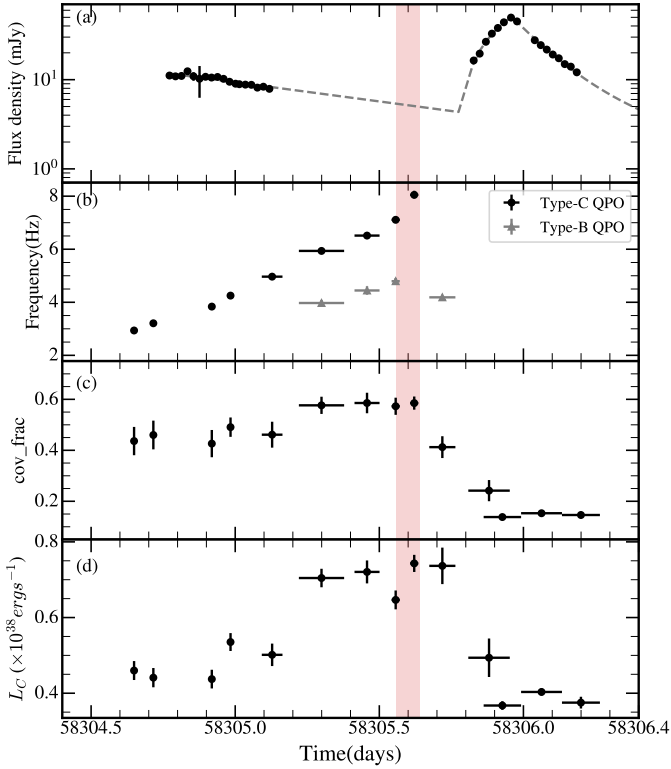


**Figure 8.** (a) AMI-LA radio light curve (15.5 GHz) from [Bright et al. \(2020\)](#) around the transient jet ejection. The grey dashed line indicates the best-fitting model from [Homan et al. \(2020\)](#): an exponential function for the baseline decay, an additional linear function for the radio flare rise, and an additional power-law function for the radio flare decay phase. (b) The concurrent evolution of the centroid frequency of type-C and type-B QPOs. The red shadows mark the transient jet ejection time on MJD  $58305.60 \pm 0.04$  according to [\(Wood et al. 2021\)](#). (c) The concurrent evolution of the cover fraction  $\text{cov\_frac}$ . (d) The concurrent evolution of the Comptonization luminosity  $L_C$  (0.1–100 keV).

rising HS, which is similar to HID ([Figure 1](#)). We have also gathered data from several outbursts with extensive observations that span the full duration of the outburst from the literature ([Sobczak et al. 2000](#); [Debnath et al. 2008](#); [McClintock et al. 2009](#)). We found that  $L_X$  and  $\Gamma$  follow a roughly “q”-like track in all three outbursts similar to the HID (see [Figure C3](#)). The data in the hard state (right part of the “q”) roughly follows a “v”-like correlation, aligning with previous work (e.g. [Yang et al. 2015](#); [Yan et al. 2020](#)). The significant scatter of the right branch of “v”-like correlation (e.g. Fig.2 in [Yan et al. 2020](#)) is evidently due to the different bend points at the upper right of the “q” track in different outbursts, i.e., the luminosity where the HS can reach.

In the case of thermal Comptonization scenario, the photon index  $\Gamma$  monotonically decreases with  $L_{\text{corona}}/L_{\text{seed}}$  (e.g. [Haardt & Maraschi 1991](#); [Beloborodov 1999](#)). The relationship in this work indeed shows the negative correlation anticipated by the model from [Beloborodov \(1999\)](#) (see [Figure C2](#)). We then present the relationship between the  $L_X$  and the ratio of  $L_C$  to  $L_{\text{seed}}$  in [Figure 4b](#). The  $L_{\text{seed}}$  is calculated by multiplying the intrinsic  $L_D$  with  $\text{cov\_frac}$ . This diagram also presents a “q”-like pattern similar to HID and  $L_X$ - $\Gamma$  including the “h”-like track during the rising HS, which is consistent with the expectation of thermal Comptonization scenario ([Beloborodov 1999](#)).

However, the reflection radiation is strong during the rising HS. So the seed photons should be dominated by the reprocessed emission from the accretion disk rather than the intrinsic disk emission ([Zdziarski et al. 1999](#); [Beloborodov 1999](#)). We cannot distinguish the reprocessed and intrinsic disk emission from current spectral fitting. In the convolution model `thcomp*kerrd` we used in the rising HS, the disk emission serves as seed photons for Compton scattering, therefore, the best-fitting parameters of disk component may not represent the true standard thin disk.

The H-S transition luminosity during the outburst rise is usually several times larger than the S-H transition luminosity during the outburst decay (e.g. [Yu & Yan 2009](#); [Tetarenko et al. 2016](#)), even the hardness ratio or photon index is similar. This phenomenon is called hysteresis effect, which is universal in outbursts experiencing state transitions (e.g. [Maccarone 2003](#)). The transition luminosities of H-S and S-H correspond to the last observation in rising HS and the first observation in decaying HS. For MAXI J1820+070, the H-S transition luminosity is  $3.32 \times 10^{37} \text{ erg s}^{-1}$ , which is almost two times higher than the S-H transition luminosity ( $1.49 \times 10^{37} \text{ erg s}^{-1}$ , see also [Figure 4](#)). The Compton luminosity of H-S transition is also roughly two times higher than that of S-H transition ( $2.73 \times 10^{37}$  and  $1.37 \times 10^{37} \text{ erg s}^{-1}$ ), while the disk luminosities are similar ( $1.17 \times 10^{36}$  and  $1.23 \times 10^{36}$ ). So the discrepancy of the transition luminosity is dominated by the Compton component.

Hot accretion flow is the predominant model to produce the Compton component during the HS (see reviews by [Yuan & Narayan 2014](#); [Liu & Qiao 2022](#)). In such a framework, the hot accretion flows can only exist below the critical luminosity  $L < \alpha^2 L_{\text{Edd}}$  (e.g. [Esin et al. 1997](#); [Xie & Yuan 2012](#)), where the  $\alpha$  is the viscosity parameter of hot accretion flow and the  $L_{\text{Edd}}$  is the Eddington luminosity. So an increasing  $\alpha$  can maintain the hot accretion flow at a high luminosity regime, to make the H-S transition luminosity higher ([Begelman & Armitage 2014](#); [Cao 2016](#); [Li & Qiao 2023](#)). The enhancement of the magnetic field and/or outflow is able to increase  $\alpha$  ([Bai & Stone 2013](#); [Cao 2016](#)). Non-stationary accretion flow has been proposed to drive the H-S transition luminosity during outburst rise, i.e. the transition luminosity is higher when the mass accretion rate increases faster ([Yu et al. 2004](#); [Yu & Yan 2009](#)). As a result, the increasing  $\alpha$  may play a similar role as the proposed non-stationary accretion flow in [Yu & Yan \(2009\)](#).

Jet or its base is also an alternative origin of the Compton emission. Some X-ray spectral and timing properties during the state transition can be well explained by jet-like corona (see the discussions in subsequent sections). [Marcel et al. \(2019\)](#) has fine-tuned two independent parameters  $r_j$  and  $\dot{m}_{in}$  of the jet-accretion disk model to replicate the “q”-like evolutionary track, where  $r_j$  is the transition radius between jet and accretion disk,  $\dot{m}_{in}$  is the mass accretion at the inner disk radius. This model is quite similar to the truncated disk model ([Esin et al. 1997](#); [Done et al. 2007](#)). However, it is still unknown what mechanism drives the evolution of  $r_j$ .

## 5.2 Inner radius of accretion disk/reflected component

We used the `kerrd` to fit the thermal component in HS, IMS and SS and acquired the evolution of  $R_{in}$  (see [Figure 2a](#)). In an optically-thick disk, the effective temperature of the blackbody emission as a given radius  $r$  will be  $T_{\text{eff}}(r) = \left[ \frac{3GM\dot{M}}{8\pi\sigma r^3} \left( 1 - \sqrt{\frac{r_{in}}{r}} \right) \right]^{\frac{1}{4}}$  ([Shakura & Sunyaev 1973](#); [Makishima et al. 1986](#)), where  $G$  is the constant of gravity,  $M$  is the BH mass,  $\dot{M}$  is the mass accretion rate and  $r_{in}$  is the inner disk radius considering the effect of

inner boundary condition. Then, the maximum disk temperature is given as  $T_{\max} = (3GM\dot{M}/8\pi\sigma r_{\text{in}}^3)^{1/4} \times 6^{3/2} \times 7^{-7/4}$  (Kubota et al. 1998). Therefore, the disk luminosity is  $L_{\text{D}} \sim 4\pi R_{\text{in}}^2 \sigma T_{\max}^4 = (3GM\dot{M}R_{\text{in}}^2/2r_{\text{in}}^3) \times 6^6 \times 7^{-7}$ , where  $R_{\text{in}}$  is our spectral fitting result. So we can obtain the true inner disk radius from spectra fitting result, since  $r_{\text{in}} = 0.44 \left( \dot{M} c^2 R_{\text{in}}^2 / L_{\text{D}} \right)$  (in units of  $R_{\text{g}}$ ). During the SS, the nearly constant  $R_{\text{in}}$  and similar evolution of  $L_{\text{D}}$  and  $\dot{M}$  result to an almost unchanged  $r_{\text{in}} \sim 7R_{\text{g}}$ , which is a little bit larger than the  $R_{\text{ISCO}}$  of a low-spinning BH (Zhao et al. 2021; Guan et al. 2021). Therefore, the exponential decreasing of  $\dot{M}$  and constant  $r_{\text{in}}$  during the SS (Figure 2) is consistent with the evolution of a standard accretion disk (Shakura & Sunyaev 1973).

In the spectral fitting of the rising HS and IMS, we employed the relativistic reflection model `relxillCp` and linked the inner radius of the reflected component to the  $R_{\text{in}}$ . We then calculated the corresponding  $r_{\text{in}}$ . During the HS, the  $r_{\text{in}}$  continuously decreases, and then increases after entering the IMS (Figure A2). The lowest  $r_{\text{in}}$  around MJD 58290 is  $4.5R_{\text{g}}$ . It is odd that the inner disk radius increases following the transition to IMS, yet the values observed afterward are smaller compared to those during the SS (Figure 2). We also used another model to fit the broadband X-ray spectra. Although the values of inner disk radius during the HS and IMS are different from `kerred`, the evolutions are similar (see section A). Especially the inner radius experiences a dip during the IMS, the value of which is lower than that in the SS (Figure A2, see also Motta et al. 2009).

The observational results present a significant challenge to our current understanding of the accretion flow evolution during the IMS, a topic that remains highly debated. On one hand, current spectral models may require refinement to accurately describe the broad-band X-ray spectra observed around IMS. On the other hand, the thermal component may not be an accretion disk. Instead, the  $R_{\text{in}}$  serves as a proxy for the emission area of thermal component rather than the inner radius of accretion disk, as  $R_{\text{in}}$  is also influenced by the total flux of the thermal component. However, the nature of this component remains puzzling, especially if its size is smaller than the  $R_{\text{ISCO}}$  of the standard accretion disk. One possible candidate is the presence of cold clumps embedded within a hot accretion flow. This two-phase accretion flow at bright hard state and/or IMS has been proposed in many previous studies (e.g. Krolik 1998; Wang et al. 2012; Xie & Yuan 2012; Liska et al. 2022). Nevertheless, the radiative properties of such an accretion flow, especially the characteristics of the cold clumps, remain poorly understood. Further investigation is required to clarify whether it can account for the X-ray spectral evolution around IMS.

We also noticed that the evolution of  $R_{\text{in}}$  is roughly consistent with the time lag between the soft and hard X-ray variability (e.g. Wang et al. 2021; De Marco et al. 2021; Echiburú-Trujillo et al. 2024). The soft lag is interpreted as the reverberation lag between the corona and the reflected component (Kara et al. 2019; Wang et al. 2021, 2022b, e.g.). The decreasing of soft lag during the HS agrees with the expected reflection from a truncated accretion disk or a contracting corona (Kara et al. 2019; De Marco et al. 2021). The increase of soft lag during the IMS is proposed to be related to an expanding of jet or jet-like corona (Wang et al. 2021; De Marco et al. 2021). A jet-like corona is also proposed to explain the other spectral and timing properties in BHXRBs (see also Kylafis et al. 2008; You et al. 2021; Cao et al. 2022; Méndez et al. 2022; Wang et al. 2022b). Under this scenario, a jet-like corona undergoes vertical contraction and expansion, resulting in the observed decrease and increase of the soft time lag and the irradiated area.

### 5.3 Type-C QPO frequency, corona geometry and Comptonization

The type-C QPO is a predominant characteristic detected in the HS and HIMS, the oscillated photons of which are generally believed to originate from the component producing the Compton emission (e.g. Lee & Miller 1998; Psaltis & Norman 2000; Bellavita et al. 2022; Ma et al. 2021; Gao et al. 2023). So it is important to investigate the QPO properties and the spectral parameters of Compton component. The correlation between the QPO frequency  $\nu_{\text{C,QPO}}$  and the photon index  $\Gamma$  of the Compton component has been widely studied (e.g. Vignarca et al. 2003; Shaposhnikov & Titarchuk 2009; Stiele et al. 2013; Wang et al. 2022a). The  $\nu_{\text{C,QPO}}$  usually positively correlates with the  $\Gamma$  over two orders of magnitude frequency range, and the  $\Gamma$  becomes saturated above a certain frequency in few sources (e.g. Vignarca et al. 2003; Shaposhnikov & Titarchuk 2009). It is generally believed that the mass accretion rate drives the evolution of both X-ray spectral and timing properties of BHXRB (see reviews in Done et al. 2007; Gilfanov 2010). The  $\Gamma$  and the  $\nu_{\text{C,QPO}}$  both increase with X-ray luminosity, resulting in a positive correlation (e.g. Revnivtsev et al. 2001; Mereminskiy et al. 2019; Wang et al. 2022a). However,  $\nu_{\text{C,QPO}}$  in MAXI J1820+070 displays a complex correlation with  $L_{\text{X}}$  (Figure 7a), and  $\Gamma$  exhibits a “ $\eta$ ”-like track along  $L_{\text{X}}$  during HS (Figure 4). These results suggest that the mass accretion rate is not the only factor influencing the evolution of the spectral and timing properties of the corona.

MAXI J1820+070 also shows a positive correlation between  $\nu_{\text{C,QPO}}$  and  $\Gamma$  with varying slopes across different phases of HS and HIMS (Figure 7b). The  $\nu_{\text{C,QPO}}$  and  $\tau$  roughly exhibit a negative correlation with a large scatter (Figure 7c). These correlations provide compelling evidence that the Comptonization is the driving force behind the evolution of the QPO frequency. Recently, some models have been proposed to explain the properties of the type-C QPO based on the Comptonization process (e.g. Bellavita et al. 2022; Mastichiadis et al. 2022). Specifically, the interplay between thermal and Compton components, which influences optical depth and electron temperature during Comptonization, can produce an oscillation roughly consistent with type-C QPO (Mastichiadis et al. 2022).

In some other models, the QPO frequency is usually thought to inversely correlate to the characteristic scale of the corona and/or the inner radius of the accretion disk (e.g. Ingram et al. 2009; Cabanac et al. 2010; Marcel et al. 2020; Rawat et al. 2023; Motta & Belloni 2024). So the increasing of QPO frequency during the rise and plateau phases of HS (Figure 6) can be accounted for the shrinking of the inner radius of a truncated accretion disk (De Marco et al. 2021; Zdziarski et al. 2021) or a contracting corona (Kara et al. 2019; Wang et al. 2021, 2022b). However, the observed decrease in QPO frequency during the bright decline, and its subsequent increase during the IMS (Figure 6), is challenging to be explained by the behavior of a contracting and then expanding jet-like corona inferred from the soft lag and X-ray spectral evolution (Wang et al. 2022b), and also contradicts with the evolution of inner disk radius under a truncated disk scenario.

The QPO frequency may alternatively be proportional to a characteristic timescale for ejecting mass as a damped oscillator in a jet-like corona model. As a result, the  $\nu_{\text{C,QPO}} \propto R_0^2 n_{e,0}$  (Kylafis et al. 2008), where the  $R_0$  is the jet base, and  $n_{e,0}$  is the electron number density of the jet base. The expanding jet-like corona during the IMS naturally causes the rapid increase of the QPO frequency. The optical depth in such corona should also be a function of  $R_0$  and  $n_{e,0}$ . However, the specific relation between  $\tau$  and  $\Gamma$  in the jet-like

corona should be investigated in order to quantitatively understand the correlations between  $\nu_{C,QPO}$  and  $\tau/\Gamma$ .

#### 5.4 The association between rapid state transition and transient jet ejection

It is widely recognized that transient jet ejections are associated with X-ray spectral state transitions (Fender et al. 2004), wherein Compton-dominated spectra shift to thermal dominated spectra. The well-sampled observations of MAXI J1820+070 offer a unique opportunity to investigate the connection between ejection event and spectral state transition. Remarkably, the last detection of type-C QPO coincided precisely with the ejection time within one hour. Subsequent to this ejection, the Compton luminosity sharply decreased by a factor of two within 8 hours. So the observations of MAXI J1820+070 establish a coincidence between the corona and ejection within timescale of hours (see also Homan et al. 2020), which the corona is responsible for the Compton emission and the type-C QPO. One plausible scenario is that the corona or part of the corona is ejected, subsequently allowing the disk component to dominate the X-ray spectrum. The dominance of ions in the ejection composition further supports this hypothesis (Zdziarski & Heinz 2024). On the other hand, Ma et al. (2023a) also proposed a double corona model, while the larger corona transforms into a vertical jet-like corona at the ejection time. Additionally, the corona transforming into an ejected jet has been proposed in the microquasar GRS 1915+105 (Mirabel et al. 1998; Méndez et al. 2022). A similar scenario has also been proposed for the active galactic nuclei (AGNs) harboring super-massive BH, such as 3C 120 (Marscher et al. 2002) and 3C 111 (Chatterjee et al. 2011), in which the observed X-ray dips are associated with the radio jet ejections.

#### ACKNOWLEDGEMENTS

We would like to thank the helpful discussion with Bei You, Fuguo Xie and Phil Uttley. This work made use of the data from Insight-HXMT mission, a project funded by China National Space Administration (CNSA) and the Chinese Academy of Sciences (CAS). This work was supported in part by the Natural Science Foundation of China (grants 12373049, U1938114, 12361131579, U1838203 and 12373050).

#### DATA AVAILABILITY

The *Insight-HXMT* and *NICER* data underlying this article are available in the public archive <http://archive.hxmt.cn/proposal> and <https://heasarc.gsfc.nasa.gov/docs/archive.html>.

#### REFERENCES

Atri P., et al., 2020, *MNRAS*, **493**, L81  
 Axelsson M., Done C., 2016, *MNRAS*, **458**, 1778  
 Baglio M. C., Russell D. M., Lewis F., 2018, *The Astronomer's Telegram*, **11418**, 1  
 Bai X.-N., Stone J. M., 2013, *ApJ*, **767**, 30  
 Basak R., Zdziarski A. A., 2016, *MNRAS*, **458**, 2199  
 Begelman M. C., Armitage P. J., 2014, *ApJ*, **782**, L18  
 Bellavita C., García F., Méndez M., Karpouzas K., 2022, *MNRAS*, **515**, 2099

Belloni T. M., 2010, in Belloni T., ed., , Vol. 794, *Lecture Notes in Physics*, Berlin Springer Verlag, Springer-Verlag Berlin Heidelberg, p. 53, doi:10.1007/978-3-540-76937-8\_3  
 Belloni T. M., Motta S. E., 2016, in Bambi C., ed., *Astrophysics and Space Science Library* Vol. 440, *Astrophysics of Black Holes: From Fundamental Aspects to Latest Developments*. p. 61 (arXiv:1603.07872), doi:10.1007/978-3-662-52859-4\_2  
 Belloni T., Psaltis D., van der Klis M., 2002, *ApJ*, **572**, 392  
 Beloborodov A. M., 1999, *ApJ*, **510**, L123  
 Bright J., Fender R., Motta S., 2018, *The Astronomer's Telegram*, **11420**, 1  
 Bright J. S., et al., 2020, *Nature Astronomy*, **4**, 697  
 Buchner J., 2021, *The Journal of Open Source Software*, **6**, 3001  
 Buisson D., Fabian A., Alston W., Walton D., Kara E., García J., Homan J., Tomsick J., 2018, *The Astronomer's Telegram*, **11578**, 1  
 Buisson D. J. K., et al., 2019, *MNRAS*, **490**, 1350  
 Buisson D. J. K., et al., 2021, *MNRAS*, **500**, 3976  
 Cabanac C., Henri G., Petrucci P. O., Malzac J., Ferreira J., Belloni T. M., 2010, *MNRAS*, **404**, 738  
 Cao X., 2016, *ApJ*, **817**, 71  
 Cao X., et al., 2020, *Science China Physics, Mechanics, and Astronomy*, **63**, 249504  
 Cao Z., Lucchini M., Markoff S., Connors R. M. T., Grinberg V., 2022, *MNRAS*, **509**, 2517  
 Casella P., Belloni T., Homan J., Stella L., 2004, *A&A*, **426**, 587  
 Chatterjee R., et al., 2011, *ApJ*, **734**, 43  
 Chen W., Shrader C. R., Livio M., 1997, *ApJ*, **491**, 312  
 Chen Y., et al., 2020, *Science China Physics, Mechanics, and Astronomy*, **63**, 249505  
 Clavel M., Rodriguez J., Corbel S., Coriat M., 2016, *Astronomische Nachrichten*, **337**, 435  
 Corral-Santana J. M., Casares J., Muñoz-Darias T., Bauer F. E., Martínez-Pais I. G., Russell D. M., 2016, *A&A*, **587**, A61  
 Dauser T., García J., Walton D. J., Eikmann W., Kallman T., McClintock J., Wilms J., 2016, *A&A*, **590**, A76  
 Dauser T., García J. A., Joyce A., Licklederer S., Connors R. M. T., Ingram A., Reynolds C. S., Wilms J., 2022, *MNRAS*, **514**, 3965  
 De Marco B., Ponti G., Muñoz-Darias T., Nandra K., 2015, *ApJ*, **814**, 50  
 De Marco B., Zdziarski A. A., Ponti G., Migliori G., Belloni T. M., Segovia Otero A., Dzielak M. A., Lai E. V., 2021, *A&A*, **654**, A14  
 Debnath D., Chakrabarti S. K., Nandi A., Mandal S., 2008, *Bulletin of the Astronomical Society of India*, **36**, 151  
 Denisenko D., 2018, *The Astronomer's Telegram*, **11400**, 1  
 Dias S. D., Vaughan S., Lefkir M., Wynn G., 2024, *MNRAS*, **529**, 1752  
 Done C., Gierliński M., Kubota A., 2007, *A&ARv*, **15**, 1  
 Dzielak M. A., De Marco B., Zdziarski A. A., 2021, *MNRAS*, **506**, 2020  
 Ebisawa K., Życki P., Kubota A., Mizuno T., Watarai K.-y., 2003, *ApJ*, **597**, 780  
 Echiburú-Trujillo C., et al., 2024, *ApJ*, **962**, 116  
 Esin A. A., McClintock J. E., Narayan R., 1997, *ApJ*, **489**, 865  
 Espinasse M., et al., 2020, *ApJ*, **895**, L31  
 Fabian A. C., et al., 2020, *MNRAS*, **493**, 5389  
 Fan N., et al., 2024, *ApJ*, **969**, 61  
 Fender R. P., Belloni T. M., Gallo E., 2004, *MNRAS*, **355**, 1105  
 Gao C., Yan Z., Yu W., 2023, *MNRAS*, **520**, 5544  
 García J., et al., 2014, *ApJ*, **782**, 76  
 Gilfanov M., 2010, in Belloni T., ed., , Vol. 794, *Lecture Notes in Physics*, Berlin Springer Verlag, p. 17, doi:10.1007/978-3-540-76937-8\_2  
 Gilfanov M., Churazov E., Revnivtsev M., 2000, *MNRAS*, **316**, 923  
 Guan J., et al., 2021, *MNRAS*, **504**, 2168  
 Haardt F., Maraschi L., 1991, *ApJ*, **380**, L51  
 Homan J., et al., 2020, *ApJ*, **891**, L29  
 Ingram A., Done C., 2012, *MNRAS*, **419**, 2369  
 Ingram A., Done C., Fragile P. C., 2009, *MNRAS*, **397**, L101  
 Ingram A., van der Klis M., Middleton M., Done C., Altamirano D., Heil L., Uttley P., Axelsson M., 2016, *MNRAS*, **461**, 1967  
 Kara E., et al., 2019, *Nature*, **565**, 198  
 Kawamura T., Done C., Axelsson M., Takahashi T., 2023, *MNRAS*, **519**, 4434

- Kawamuro T., et al., 2018, *The Astronomer's Telegram*, [11399, 1](#)
- Krolik J. H., 1998, *ApJ*, [498, L13](#)
- Kubota A., Tanaka Y., Makishima K., Ueda Y., Dotani T., Inoue H., Yamaoka K., 1998, *PASJ*, [50, 667](#)
- Kylafis N. D., Papadakis I. E., Reig P., Giannios D., Pooley G. G., 2008, *A&A*, [489, 481](#)
- Leahy D. A., Darbro W., Elsner R. F., Weisskopf M. C., Sutherland P. G., Kahn S., Grindlay J. E., 1983, *ApJ*, [266, 160](#)
- Lee H. C., Miller G. S., 1998, *MNRAS*, [299, 479](#)
- Li J., Qiao E., 2023, *MNRAS*, [521, 3237](#)
- Liska M. T. P., Musoke G., Tchekhovskoy A., Porth O., Beloborodov A. M., 2022, *ApJ*, [935, L1](#)
- Liu B. F., Qiao E., 2022, *iScience*, [25, 103544](#)
- Liu C., et al., 2020, *Science China Physics, Mechanics, and Astronomy*, [63, 249503](#)
- Ma X., et al., 2021, *Nature Astronomy*, [5, 94](#)
- Ma R., Méndez M., García F., Sai N., Zhang L., Zhang Y., 2023a, *MNRAS*, [525, 854](#)
- Ma X., et al., 2023b, *ApJ*, [948, 116](#)
- Maccarone T. J., 2003, *A&A*, [409, 697](#)
- Makishima K., Maejima Y., Mitsuda K., Bradt H. V., Remillard R. A., Tuohy I. R., Hoshi R., Nakagawa M., 1986, *ApJ*, [308, 635](#)
- Marcel G., et al., 2019, *A&A*, [626, A115](#)
- Marcel G., et al., 2020, *A&A*, [640, A18](#)
- Marscher A. P., Jorstad S. G., Gómez J.-L., Aller M. F., Teräsranta H., Lister M. L., Stirling A. M., 2002, *Nature*, [417, 625](#)
- Mastichiadis A., Petropoulou M., Kylafis N. D., 2022, *A&A*, [662, A118](#)
- McClintock J. E., Remillard R. A., Rupen M. P., Torres M. A. P., Steeghs D., Levine A. M., Orosz J. A., 2009, *ApJ*, [698, 1398](#)
- Méndez M., Karpouzias K., García F., Zhang L., Zhang Y., Belloni T. M., Altamirano D., 2022, *Nature Astronomy*, [6, 577](#)
- Mereminskiy I. A., Semena A. N., Bykov S. D., Filippova E. V., Lutovinov A. A., Poutanen J., 2019, *MNRAS*, [482, 1392](#)
- Mirabel I. F., Dhawan V., Chaty S., Rodriguez L. F., Marti J., Robinson C. R., Swank J., Geballe T., 1998, *A&A*, [330, L9](#)
- Motta S. E., Belloni T. M., 2024, *A&A*, [684, A209](#)
- Motta S., Belloni T., Homan J., 2009, *MNRAS*, [400, 1603](#)
- Motta S., Muñoz-Darias T., Casella P., Belloni T., Homan J., 2011, *MNRAS*, [418, 2292](#)
- Motta S., Homan J., Muñoz Darias T., Casella P., Belloni T. M., Hiemstra B., Méndez M., 2012, *MNRAS*, [427, 595](#)
- Mudambi S. P., Maqbool B., Misra R., Hebbar S., Yadav J. S., Gudennavar S. B., S. G. B., 2020, *ApJ*, [889, L17](#)
- Mummery A., Ingram A., Davis S., Fabian A., 2024, *MNRAS*, [531, 366](#)
- Muno M. P., Morgan E. H., Remillard R. A., 1999, *ApJ*, [527, 321](#)
- Nathan E., et al., 2022, *MNRAS*, [511, 255](#)
- Novikov I. D., Thorne K. S., 1973, in *Black Holes (Les Astres Occlus)*. pp 343–450
- Peng J. Q., et al., 2023, *MNRAS*, [518, 2521](#)
- Psaltis D., Norman C., 2000, *arXiv e-prints*, [pp astro-ph/0001391](#)
- Rawat D., Husain N., Misra R., 2023, *MNRAS*, [524, 5869](#)
- Remillard R. A., McClintock J. E., 2006, *ARA&A*, [44, 49](#)
- Revnivtsev M., Gilfanov M., Churazov E., 2001, *A&A*, [380, 520](#)
- Shakura N. I., Sunyaev R. A., 1973, *A&A*, [24, 337](#)
- Shaposhnikov N., Titarchuk L., 2009, *ApJ*, [699, 453](#)
- Shappee B. J., et al., 2014, *ApJ*, [788, 48](#)
- Shidatsu M., Nakahira S., Murata K. L., Adachi R., Kawai N., Ueda Y., Negoro H., 2019, *ApJ*, [874, 183](#)
- Shimura T., Takahara F., 1995, *ApJ*, [445, 780](#)
- Sobczak G. J., McClintock J. E., Remillard R. A., Cui W., Levine A. M., Morgan E. H., Orosz J. A., Bailyn C. D., 2000, *ApJ*, [544, 993](#)
- Stevens A. L., Uttley P., 2016, *MNRAS*, [460, 2796](#)
- Stiele H., Kong A. K. H., 2020, *ApJ*, [889, 142](#)
- Stiele H., Yu W., 2015, *MNRAS*, [452, 3666](#)
- Stiele H., Belloni T. M., Kalemci E., Motta S., 2013, *MNRAS*, [429, 2655](#)
- Sunyaev R. A., Truemper J., 1979, *Nature*, [279, 506](#)
- Tetarenko B. E., Sivakoff G. R., Heinke C. O., Gladstone J. C., 2016, *ApJS*, [222, 15](#)
- Torres M. A. P., Casares J., Jiménez-Ibarra F., Álvarez-Hernández A., Muñoz-Darias T., Armas Padilla M., Jonker P. G., Heida M., 2020, *ApJ*, [893, L37](#)
- Tucker M. A., et al., 2018, *ApJ*, [867, L9](#)
- Uttley P., Cackett E. M., Fabian A. C., Kara E., Wilkins D. R., 2014, *A&ARv*, [22, 72](#)
- Uttley P., et al., 2018, *The Astronomer's Telegram*, [11423, 1](#)
- Vignarca F., Migliari S., Belloni T., Psaltis D., van der Klis M., 2003, *A&A*, [397, 729](#)
- Wang J.-M., Cheng C., Li Y.-R., 2012, *ApJ*, [748, 147](#)
- Wang Y., et al., 2020, *ApJ*, [896, 33](#)
- Wang J., et al., 2021, *ApJ*, [910, L3](#)
- Wang P. J., et al., 2022a, *MNRAS*, [512, 4541](#)
- Wang J., et al., 2022b, *ApJ*, [930, 18](#)
- Wood C. M., et al., 2021, *MNRAS*, [505, 3393](#)
- Xie F.-G., Yuan F., 2012, *MNRAS*, [427, 1580](#)
- Xu Y., Harrison F. A., Tomsick J. A., Hare J., Fabian A. C., Walton D. J., 2020, *ApJ*, [893, 42](#)
- Yan Z., Yu W., 2015, *ApJ*, [805, 87](#)
- Yan Z., Xie F.-G., Zhang W., 2020, *ApJ*, [889, L18](#)
- Yang Q.-X., Xie F.-G., Yuan F., Zdziarski A. A., Gierliński M., Ho L. C., Yu Z., 2015, *MNRAS*, [447, 1692](#)
- You B., et al., 2021, *Nature Communications*, [12, 1025](#)
- You B., Dong Y., Yan Z., Liu Z., Tuo Y., Yao Y., Cao X., 2023, *ApJ*, [945, 65](#)
- Yu W., Yan Z., 2009, *ApJ*, [701, 1940](#)
- Yu W., van der Klis M., Fender R., 2004, *ApJ*, [611, L121](#)
- Yuan F., Narayan R., 2014, *ARA&A*, [52, 529](#)
- Zdziarski A. A., Heinz S., 2024, *ApJ*, [967, L7](#)
- Zdziarski A. A., Johnson W. N., Magdziarz P., 1996, *MNRAS*, [283, 193](#)
- Zdziarski A. A., Lubiński P., Smith D. A., 1999, *MNRAS*, [303, L11](#)
- Zdziarski A. A., Dzielak M. A., De Marco B., Szanecki M., Niedźwiecki A., 2021, *ApJ*, [909, L9](#)
- Zdziarski A. A., You B., Szanecki M., Li X.-B., Ge M., 2022, *ApJ*, [928, 11](#)
- Zhang S.-N., et al., 2020, *Science China Physics, Mechanics, and Astronomy*, [63, 249502](#)
- Zhao X., et al., 2021, *ApJ*, [916, 108](#)
- van der Klis M., 1989, in Ögelman H., van den Heuvel E. P. J., eds, *NATO Advanced Study Institute (ASI) Series C Vol. 262, Timing Neutron Stars*. p. 27, [doi:10.1007/978-94-009-2273-0\\_3](#)

## APPENDIX A: SPECTRAL FITTING RESULTS OF A REPLACED MODEL FOR THE RISING HS

In order to verify the spectral parameters evolution, we have applied another model to describe the spectra observed in the rising HS and IMS, which is `constant*TBabs*(diskbb+relxillCp+xillverCp)`. The `diskbb` is a multi-blackbody component representing the accretion disk radiation. We used `relxillCp` to fit the Comptonization emission and the relativistic reflection emission. Furthermore, the same equivalent hydrogen column density, black hole spin, inclination angle and distance were maintained. However, the reflection fraction `refl_frac` is free, which represents the ratio of emitted photons from the corona illuminating the disk to the fraction of photons towards the observers (Dauser et al. 2016). It is worthy noting that we tied the normalization  $N_{\text{disk}}$  of the `diskbb` to the inner disk radius  $R_{\text{in}}$  (in units of  $R_g$ ) in `relxillCp` as  $816R_{\text{in}}^2$  (Gao et al. 2023) since  $N_{\text{disk}} = (\frac{R_{\text{in}}/1\text{km}}{D/10\text{kpc}})^2 \cos i$  (Kubota et al. 1998; Basak & Zdziarski 2016). During and after the soft state, we applied the model `constant*TBabs*(diskbb+nthComp)` to fit the broadband X-ray spectrum.

The evolution of the main parameters of these models is present in Figure A1. We can find the same parameters have almost similar evolution to the results in the main text. The reflection fraction  $R_f$  increases in the rise phase of HS and subsequently undergoes a gradual decline until the SS. The evolution of  $R_f$  is almost identical to  $R_S$  in Figure 3, which demonstrates that they are tightly related (Dauser et al. 2016). The inner disk temperature  $T_{\text{in}}$  gradually increases until the decline phase of HS, and shows a rapid increase during the IMS, an exponential decrease during the SS.

The nearly constant  $N_{\text{disk}}$  and exponential decrease of  $T_{\text{in}}$  during the SS (Figure A1) are also consistent with a standard accretion disk that the inner radius reaches the innermost stable circular orbit  $R_{\text{ISCO}}$  (Shakura & Sunyaev 1973). The  $R_{\text{in}}$  derived from `diskbb` is present in Figure A2. It is clear that the evolution of  $R_{\text{in}}$  derived from `diskbb` is consistent with that from `kerrd`. Especially, there is also a dip during the transition to the IMS, and the lowest  $R_{\text{in}}$  is lower than that in the SS.

## APPENDIX B: COMPARISON OF SPECTRAL FITTINGS BETWEEN SIMULTANEOUS NICER AND INSIGHT-HXMT OBSERVATIONS

We conducted a comparative analysis of the simultaneous *NICER* and *Insight-HXMT* observations during the IMS when *Insight-HXMT* observations are absent. The evolution of the main parameters and luminosities are present in Figure B1. In these simultaneous observations, they show consistent evolutions, although the absolute values of few specific spectral fitting differ. The major discrepancies are  $\Gamma$  and  $L_R$  during the SIMS where the values derived from *NICER* are markedly higher than those from *Insight-HXMT*. The disk component becomes dominated during the SIMS (see Figure C4(f)). So the photon index derived from energy band below 10 keV (similar to *NICER* data) apparently higher than that from the entire energy band 2–150 keV.

In the HIMS, the Comptonization emission dominates the spectra (see Figure C4 (d) and (e)), thereby the fitting results are roughly consistent between two telescopes. Therefore, we believe that the fitting results from *NICER* can indeed serve as a supplement when *Insight-HXMT* observations are absent during the HIMS.

## APPENDIX C: SOME EXTRA MATERIALS

Some additional figures and tables are listed here.

This paper has been typeset from a  $\text{\TeX}/\text{\LaTeX}$  file prepared by the author.

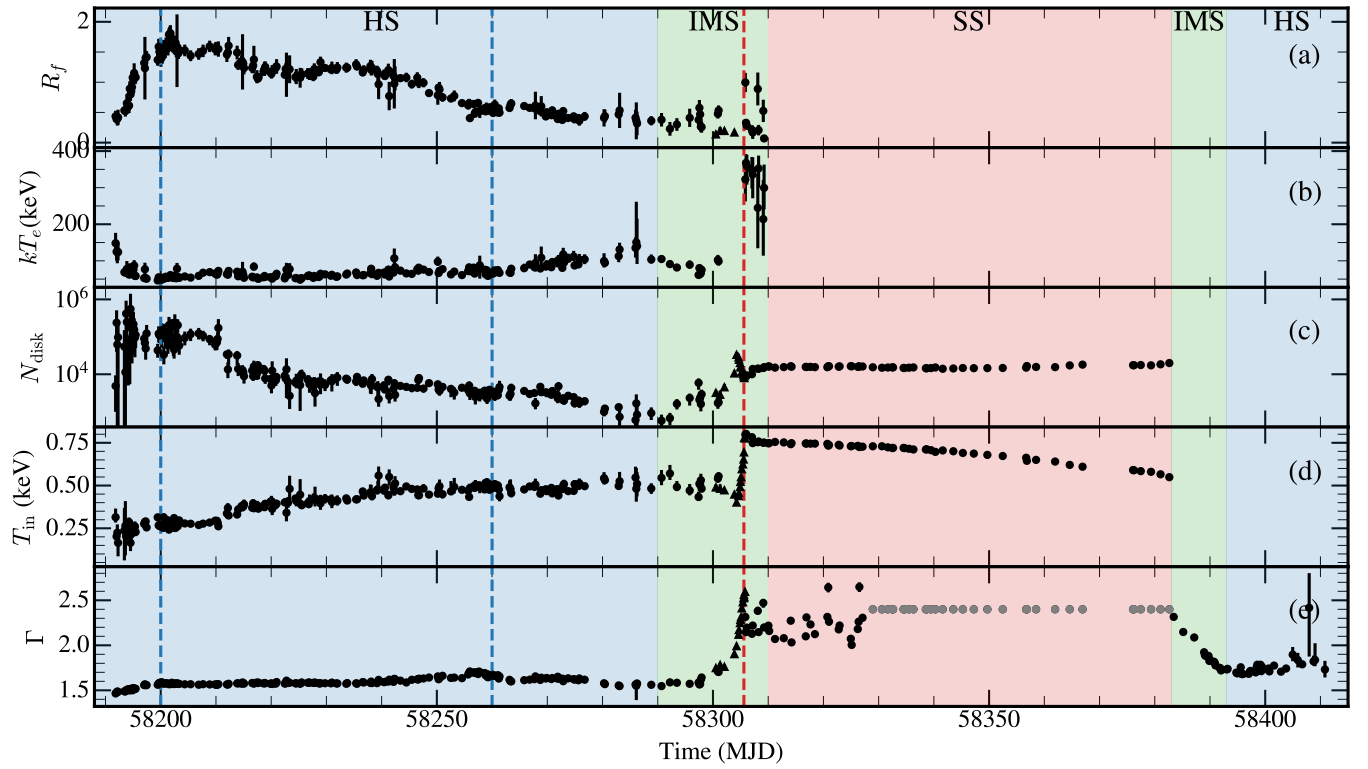


**Figure A1.** Time evolution of spectral parameters of constant\*TBabs\*(diskbb+relxillCp+xillverCp). From top to bottom: the reflection fraction  $R_f$ , the electron temperature  $kT_e$ , the normalization of the diskbb  $N_{\text{disk}}$ , the inner disk temperature  $T_{\text{in}}$ , the photon index  $\Gamma$ . The dots are derived from *Insight*-HXMT data and the triangles are derived from *NICER* data. The grey dots represent the fixed values. The colors of the background and dashed lines are the same as in Figure 1.

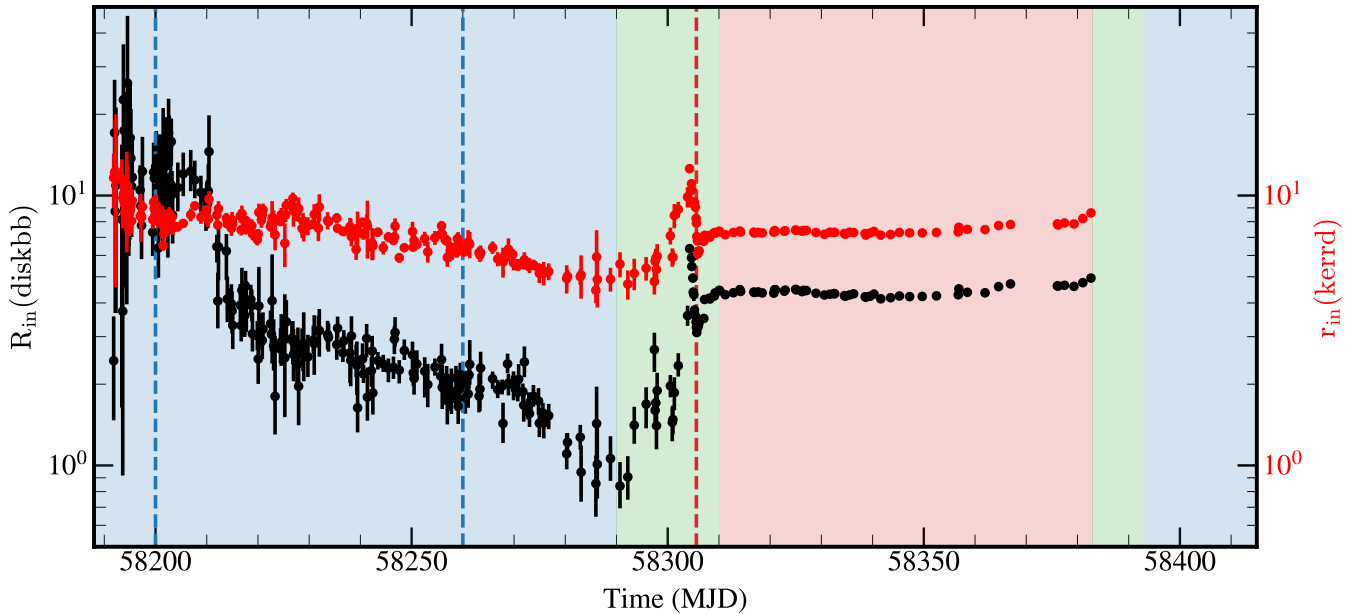


**Figure A2.** We compared the inner disk radius estimated using the diskbb (section A) and Kerrd (subsection 3.4 and subsection 5.2) models. For the black dots, the model we use is constant\*TBabs\*(diskbb+relxillCp+xillverCp) during the HS and IMS and constant\*TBabs\*(diskbb+nthComp) during the SS. For the red dots, the model is constant\*TBabs\*(thcomp\*kerrd+relxillCp+xillverCp) during the HS and same model without xillverCp during the IMS and is constant\*TBabs\*thcomp\*kerrd during SS. We have adopted a distance of 2.96kpc (Atri et al. 2020), an inclination angle of  $63^\circ$  (Atri et al. 2020), and a black hole mass of  $8.48M_\odot$  (Torres et al. 2020). Despite being derived from different models, the evolution of  $r_{\text{in}}$  appears roughly consistent.

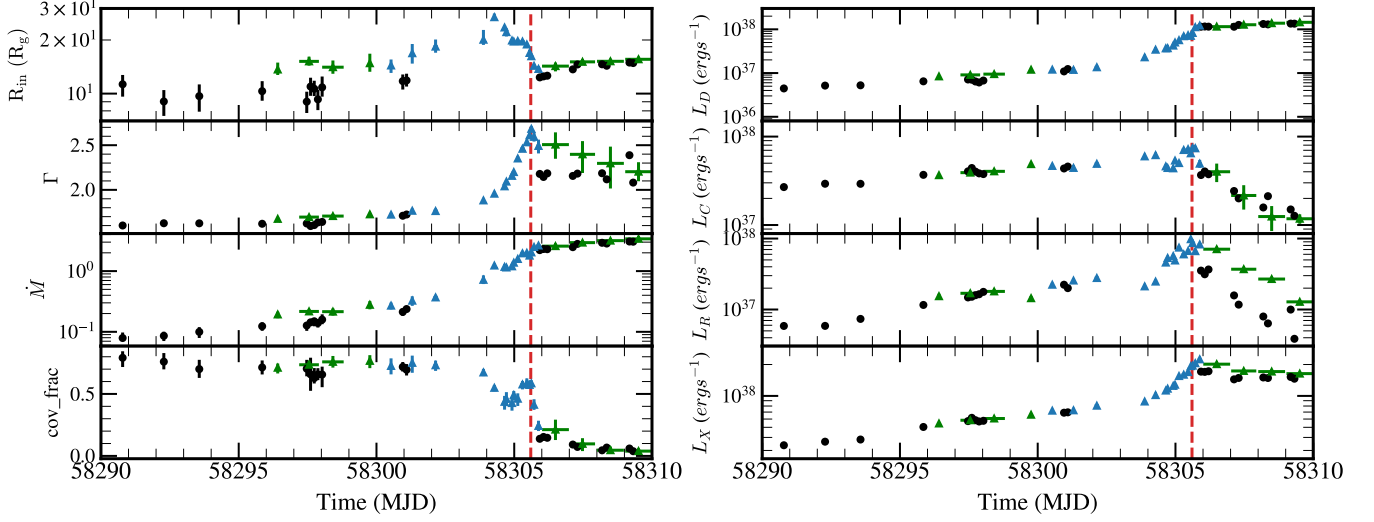


**Figure B1.** The spectral parameters and X-ray luminosities of different spectral components during the IMS when *Insight*-HXMT observations are absent. The black dots are derived from *Insight*-HXMT observations. The blue triangles are derived from *NICER* observations we used in [subsection 4.4](#) and the green triangles are derived from *NICER* observations simultaneous to *Insight*-HXMT observations. The red dashed line marks the transient jet ejection time and also the boundary between HIMS and SIMS.

**Table C1.** The QPO information of each segment in *NICER* obsID 1200120196 and 1200120197

Start (s)	End (s)	Time (MJD)	$\nu_{C,QPO}$ (Hz)	$RMS_{C,QPO}$	$Q_{C,QPO}$	$\sigma_{C,QPO}$	$\nu_{B,QPO}$ (Hz)	$RMS_{B,QPO}$	$Q_{B,QPO}$	$\sigma_{B,QPO}$
142237907.0	142238873.0	58304.2728	$2.1063^{+0.0197}_{-0.0180}$	$0.0366^{+0.0017}_{-0.0018}$	5.6347	20.7906	--	--	--	--
142269824.0	142271003.0	58304.6423	$2.9366^{+0.0201}_{-0.0208}$	$0.0277^{+0.0011}_{-0.0011}$	7.2508	24.6821	--	--	--	--
142275663.0	142276722.0	58304.7098	$3.2084^{+0.0194}_{-0.0198}$	$0.0288^{+0.0008}_{-0.0011}$	6.0187	30.1199	--	--	--	--
142292969.0	142294468.0	58304.9101	$3.8371^{+0.0361}_{-0.0368}$	$0.0217^{+0.0012}_{-0.0012}$	6.0500	17.7883	--	--	--	--
142298630.0	142300026.0	58304.9757	$4.2509^{+0.0225}_{-0.0268}$	$0.0206^{+0.0008}_{-0.0008}$	8.5140	25.8217	--	--	--	--
142308700.0	142314902.0	58305.0922	$4.9658^{+0.0324}_{-0.0344}$	$0.0161^{+0.0009}_{-0.0009}$	7.7465	18.1335	--	--	--	--
142319818.0	142333386.0	58305.2209	$5.9361^{+0.0284}_{-0.0248}$	$0.0138^{+0.0004}_{-0.0004}$	4.9696	37.6554	$3.9725^{+0.1147}_{-0.1200}$	$0.0086^{+0.0004}_{-0.0003}$	2.7874	25.1214
142336496.0	142344002.0	58305.4139	$6.514^{+0.0347}_{-0.0367}$	$0.0099^{+0.0003}_{-0.0003}$	7.3527	29.2912	$4.4448^{+0.1583}_{-0.1605}$	$0.0078^{+0.0004}_{-0.0004}$	3.2001	20.7388
142347614.0	142350064.0	58305.5426	$7.1084^{+0.0953}_{-0.0904}$	$0.0106^{+0.0007}_{-0.0007}$	3.3794	15.9888	$4.7946^{+0.1202}_{-0.1442}$	$0.0070^{+0.0005}_{-0.0005}$	5.5420	14.4097
142353173.0	142355624.0	58305.6069	$8.0492^{+0.1531}_{-0.1288}$	$0.0051^{+0.0007}_{-0.0007}$	4.4178	7.2738	--	--	--	--
142358915.0	142366743.0	58305.6734	--	--	--	--	$4.1864^{+0.0275}_{-0.0275}$	$0.0084^{+0.0003}_{-0.0004}$	5.6659	22.8935
142370610.0	142383043.0	58305.8088	--	--	--	--	--	--	--	--

Notes:

Start: the start time of segments; End: the end time of segments;  $\nu$ : centroid frequency; RMS: root mean square; Q: quality factor;  $\sigma$ : significance. The subscript B and C represent the type-B and type-C QPOs.

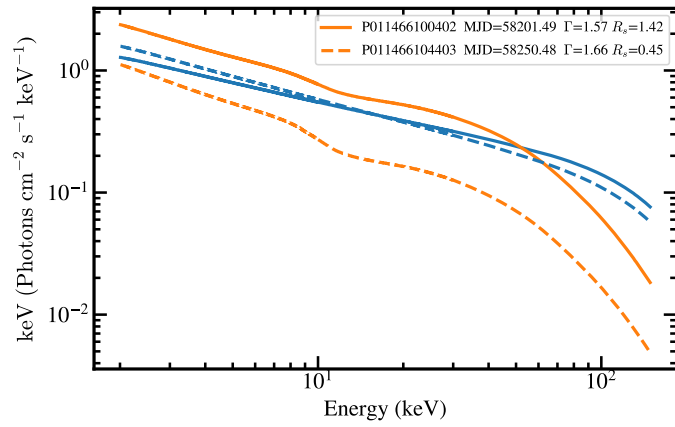


**Figure C1.** The corresponding Compton (in blue) and relativistic reflection (in orange) components of the best-fitting models under different reflection strength  $R_s$  in *Insight*-HXMT observations. The exposure ID,  $R_s$  and  $\Gamma$  are present on the upper right in the figure. It is clear that the Reflection component dominates over the Compton component when the  $R_s$  is larger than 1.

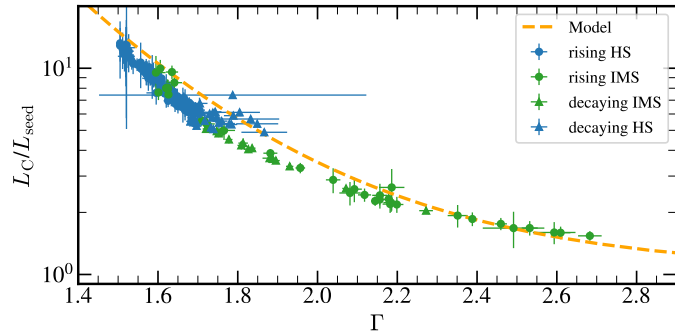
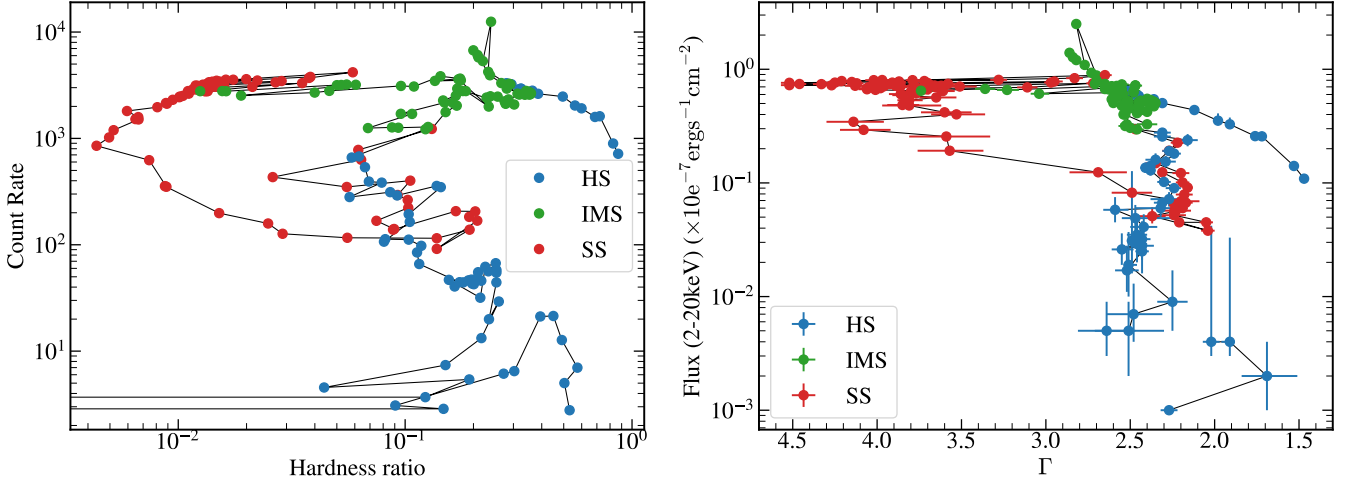
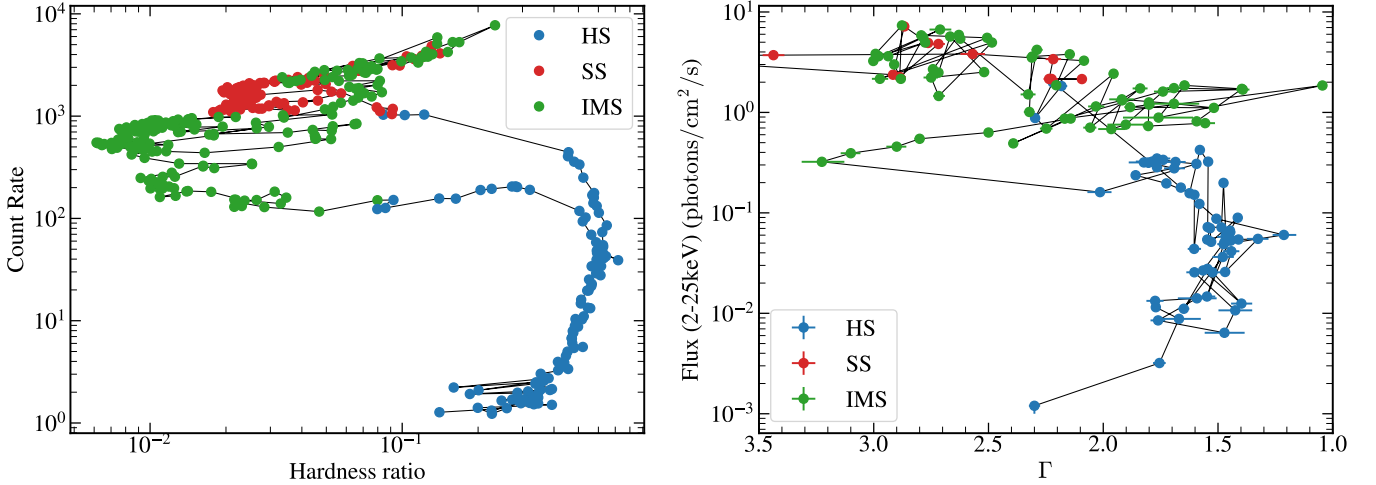


**Figure C2.** The relationship between  $\Gamma$  and the ratio of  $L_C$  to  $L_{\text{seed}}$  is consistent with the model from [Beloborodov \(1999\)](#).

## XTE J1550–564



## GRO J1655–40



## H1743–322

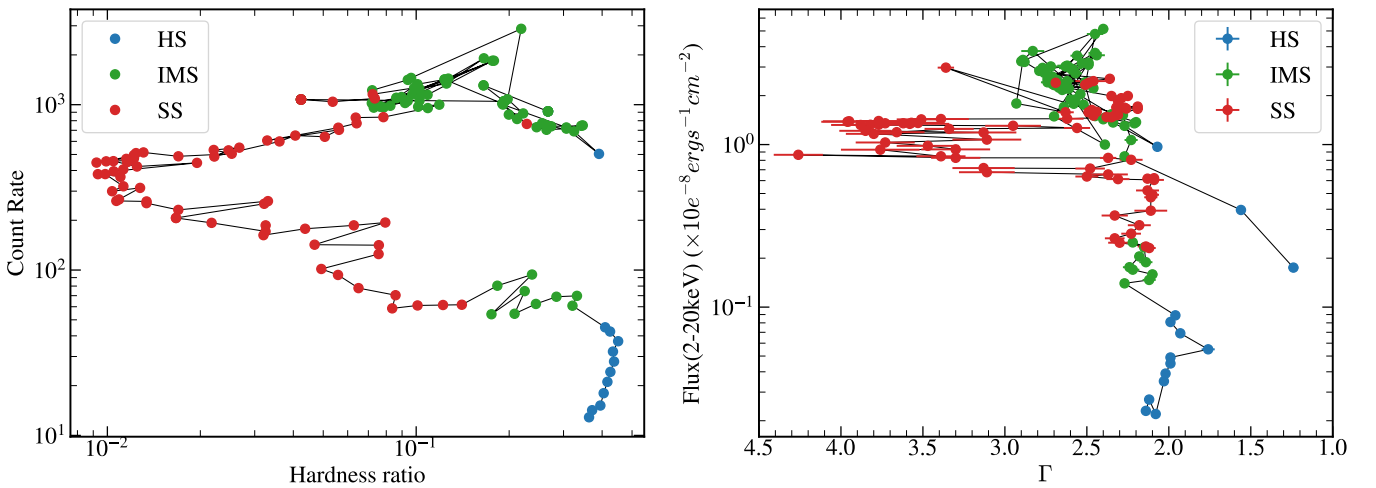


**Figure C3.** The hardness-intensity diagram (HID) and flux- $\Gamma$  plane during three outbursts in other sources, with the left panels showing the HID and the right panels showing the flux- $\Gamma$  plane. The outbursts, in order from top to bottom, are as follows: the 1998 outburst of XTE J1550–564, the 2005 outburst of GRO J1655–40 and the 2003 outburst of H1743–322. The HIDs are defined as the total 2.5–30 keV count rate vs. the ratio of hard (10–30 keV) to soft (2.5–6 keV) count rates from *RXTE/PCA*. The flux and  $\Gamma$  data are from public data in Sobczak et al. (2000); Debnath et al. (2008); McClintock et al. (2009), respectively.

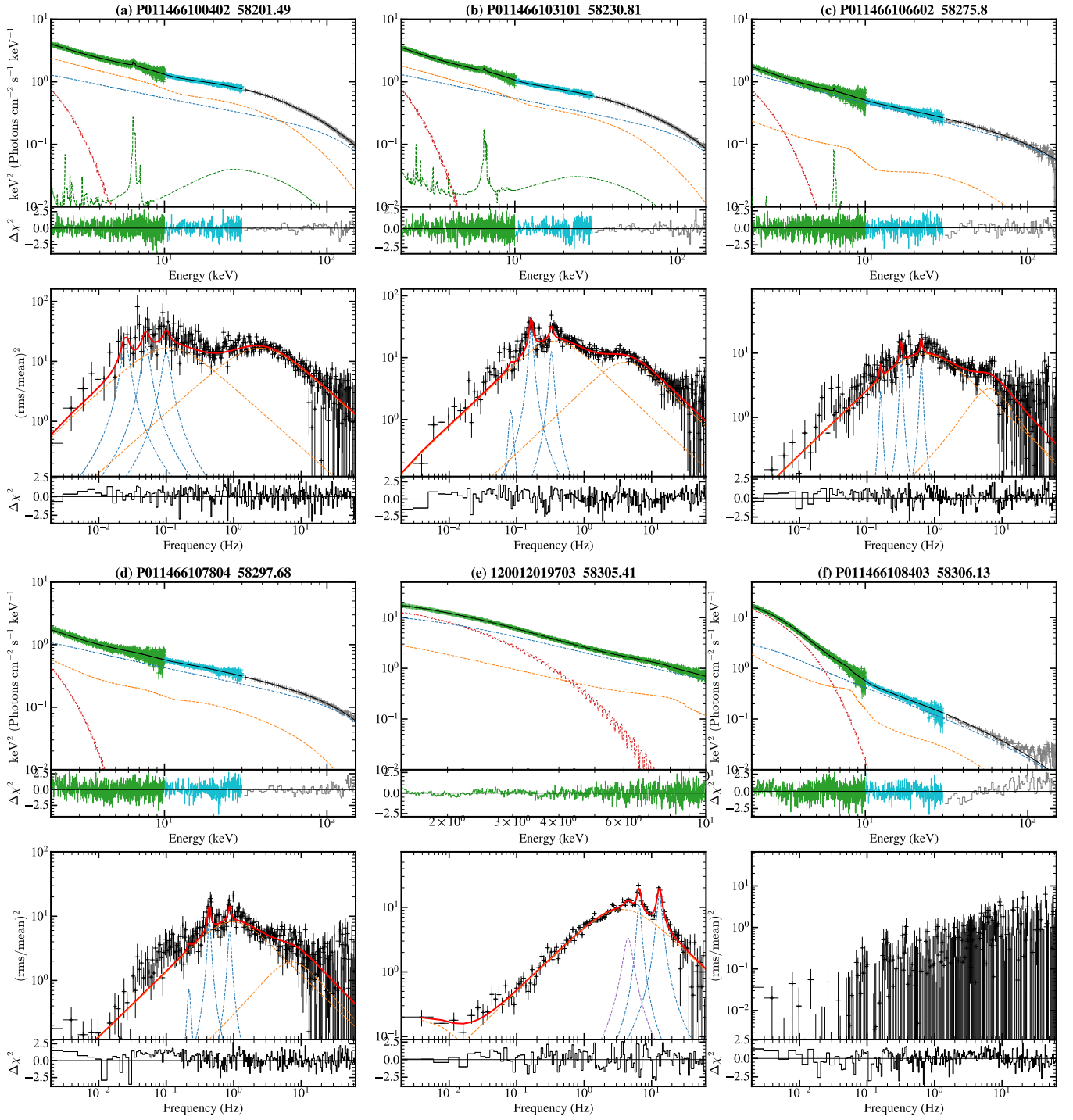


**Figure C4.** Examples of spectra and PDS for five *Insight*-HXMT observations and one *NICER* observation. These observations capture distinct phases of the HS and IMS: the rise, plateau, and bright decline during the HS and HIMS as observed by *Insight*-HXMT, the HIMS observed by *NICER*, and the SIMS. In spectra, the error bars show the data from *Insight*-HXMT LE (green), ME (cyan), HE (black) and *NICER* (green). The dashed lines show the best-fitting components: disk (red), Compton (blue), relativistic reflection (orange) and non-relativistic reflection (green) components respectively. In PDS, The dashed lines show the best-fitting components: Type-C QPO and its harmonic and/or subharmonic (blue), Type-B QPO (purple) and BLN components (orange).